Ore Geology Reviews 78 (2016) 252–267

Contents lists available at ScienceDirect

Ore Geology Reviews

journal homepage: www.elsevier.com/locate/oregeorev

Mineralogy, chalcopyrite Re−−Os geochronology and sulfur isotope of the Hujiayu Cu deposit in the Zhongtiao Mountains, North China Craton: Implications for a Paleoproterozoic metamorphogenic copper mineralization

Zheng-Jie Qiu [a,b], Hong-Rui Fan [a,b,*], Xuan Liu [a], Kui-Feng Yang [a,b], Fang-Fang Hu [a,b], Wen-Gang Xu [a], Bo-Jie Wen [a]

[a] Key Laboratory of Mineral Resources, Institute of Geology and Geophysics, Chinese Academy of Sciences, Beijing 100029, China
[b] College of Earth Science, University of Chinese Academy of Sciences, Beijing 100049, China

ARTICLE INFO

Article history:
Received 15 February 2016
Received in revised form 7 April 2016
Accepted 11 April 2016
Available online 19 April 2016

Keywords:
Metamorphogenic ore deposits
Chalcopyrite Re–Os dating
Graphite geothermometry
Clausthalite
Cobaltiferous pyrite
Zhongtiao Mountains

ABSTRACT

The Hujiayu Cu deposit, located in the Zhongtiao Mountains district of southern North China Craton, is hosted by graphite schist and dolomitic marble with disseminated to veinlet (stage I) and thick vein (stage II) mineralization. Stage I mineralization, characterized by stratabound, disseminated pyrite and chalcopyrite within the graphite schist host rock, formed at the syn-metamorphic stage. Graphite geothermometry showed that the host rock was subjected to an upper-greenschist to lower amphibolite metamorphism at a temperature range of 486 to 596 °C, averaging of 546 ± 35 °C (1 σ, n = 19). Stage II mineralization, consisting of brecciated dolomitic thick veins cemented by quartz-sulfide assemblages, was a product of metamorphic hydrothermal activity. This thick vein was subdivided into an early hydrothermal dolomitic alteration composing of dolomitic breccia with some cobaltiferous pyrite (stage IIa) and a late siliceous-copper mineralization consisting of quartz-sulfide assemblages (stage IIb). A clausthalite–siegenite–sphalerite–chalcopyrite mineral assemblage was observed in stage IIb, constraining the sulfur fugacity and selenium fugacity within −18.7 to −11.7 and −21.7 to −14.7, respectively. It was inferred stage IIb was marked by a drop in sulfur fugacity and a substantial increase in selenium fugacity after the major chalcopyrite precipitation. Calculations based on the compositions of cobaliterous pyrite and sphalerite reveal that the mineral assemblage at stage IIa formed at an approximately temperature range of 400 to 300 °C, whereas the minerals in stage IIb occurred at temperature of 256 ± 9 °C (1 σ, n = 7). Sulfides from stage I have $\delta^{34}S$ value ranging from 10.1 to 22.2‰ with an average value of 16.9 ± 3.4‰ (1 σ, n = 27), supporting the model that sulfides precipitated through thermochemical reduction of sulfate at sedimentary stage followed by metamorphic homogenization of $\delta^{34}S$ isotopic signatures. Sulfides from the stage II have $\delta^{34}S$ values in highly variable ranging from 3.4 to 19.2‰, indicating a rather complex source. Four chalcopyrite samples yielded a weighted model age of 1952 ± 39 Ma (1 σ, MSWD = 1.5), suggesting that the copper mineralization formed synchronously with regional metamorphism (1970–1850 Ma) and hence a Paleoproterozoic metamorphogenic copper mineralization is implicated. Therefore, we envisaged disseminated-veinlet mineralization formed during a metamorphic peak and the major hydrothermal copper mineralization occurred during the retrograde cooling.

1. Introduction

World-class vein-type deposits of precious and base metal ores are not uncommon in metamorphic terranes (e.g. accretionary wedge, collisional orogen, greenstone belt), and are usually interpreted to be genetically linked to regional metamorphism (e.g. Pohl, 1992; Heinrich et al., 1989; Wen et al., 1996; Pirajno, 2000; Cartwright and Oliver, 2000; Goldfarb et al., 2005; Asadi et al., 2013). They are commonly associated with metamorphic fluids characterized by near-neutral, aqueous carbonic fluids (e.g. Heinrich et al., 1989; Ridley and Diamond, 2000; Groves et al., 2003; Goldfarb et al., 2005). Pathways for metamorphic fluids may be some permeable rocks or tectonic structures in favoring of fluid flow, and the physico-chemical conditions changes (e.g. temperature/pressure dropping or fluid–rock reaction) along the pathways will induce precipitation of metal-bearing phases and formation of metamorphogenic mineral deposits (Pohl, 1992; Cartwright and Oliver, 2000). While many ore deposits are hosted in the metamorphic rocks, it is a difficult task to distinguish metamorphogenic mineral

* Corresponding author at: College of Earth Science, University of Chinese Academy of Sciences, Beijing 100049, China.
E-mail address: fanhr@mail.iggcas.ac.cn (H.-R. Fan).

http://dx.doi.org/10.1016/j.oregeorev.2016.04.007
0169-1368/

deposits and metamorphosed mineral deposits that were formed prior to the metamorphism (Marshall et al., 2000; Cartwright and Oliver, 2000; Zhong et al., 2012). An additional complicating issue is that some mineral deposits in metamorphic environments may reflect a two-stage process with initial pre-metamorphic elemental enrichment and further enrichment during metamorphism (Cartwright and Oliver, 2000). Accordingly, the age of metamorphogenic mineralization is nearly identical with the timing of metamorphism. However, precise dating of syn-metamorphic mineral deposits is a big challenge due to the lack of datable minerals that can be unequivocally linked to mineralization. Recently, the development of Re—Os dating method for low-level highly radiogenic sulfides makes it possible to delineate the direct age of mineralization (e.g. Stein et al., 2000; Qi et al., 2010).

The Zhongtiao Mountains Cu mineralizing district of North China Craton (NCC) contains several medium-size Cu deposits in the greenschist to lower amphibolite facies sedimentary rocks, commonly known as the "Hu-Bi type" Cu deposits in Chinese literatures (Hu and Sun, 1987; Sun et al., 1990). Until recently, nearly no attention has been paid to the genetic relation between metamorphism and ore formation in the district, leading to huge dispute on their genesis. Several mutually exclusive models have been forwarded, i.e., metamorphosed sedimentary exhalative model (M-Sedex, Sun et al., 1989; Zhao and Zhen, 2006), metamorphosed sediment-hosted stratiform Cu—Co deposit model (M-SSC, Zhang, 2012; Jiang et al., 2014) and remobilized sedimentary ore model (RSO, Hu and Sun, 1987; Sun et al., 1990). The M-Sedex model suggested that the deposits were formed as a result of hydrothermal deposition in submarine basin through volcanic hydrothermal exhalation and hydrothermal metasomatism. The M-SSC model stressed that the copper mineralization formed simultaneously with its host rocks and then underwent a limited degree of syn-metamorphic remobilization caused by later regional metamorphism and deformation. The RSO model favored that the original copper deposited at the time of sedimentary stage and the current copper mineralization styles were completed during metamorphism. The causative reason is lack of knowledge of metamorphic conditions and mineralizing age.

In this present contribution, we provide a comprehensive description of ore textures and chemical compositions of the host rocks and vein mineral assemblages of the Hujiayu Cu deposit, documenting the factors controlling precipitation of pyrite and the temperature evolution of sulfide precipitation. We report, for the first time, a chalcopyrite Re—Os isotopic age, which represents the timing of copper mineralization. Based on the new reliable data, the relation between Paleoproterozoic metamorphism and copper mineralization process was constructed.

2. Geological setting

The North China Craton (NCC) preserved three major Paleoproterozoic mobile belts, the Jiaoliao mobile belt in the eastern NCC, the Fengzhen mobile belt in the northern NCC, and the Jinyü mobile belt in the central southern NCC (Fig. 1a, Zhai and Santosh, 2013). The Zhongtiao Mountains copper district is situated in the southern tail of the Jinyü mobile belt, displaying broad similar correlations stratigraphic sequence with the adjacent lvliang Complex (Zhai and Peng, 2007).

The basement rocks in the Zhongtiao Mountains Cu district are composed of Neoarchean tonalite–trondhjemite–granodiorite (TTG) suite (2.7–2.5 Ga, Sun et al., 1992; Tian et al., 2006; Zhu et al., 2013; Zhang et al., 2013b), a supracrustal rock enclave with a Sm—Nd isochron age of ca. 2.5 Ga (Sun et al., 1992), and multiphase Paleoproterozoic granitoids (2.5–2.3 Ga, Sun et al., 1990; Yu et al., 2006).The Paleoproterozoic volcano-sedimentary rocks (2.2–2.0 Ga, Li et al., 2009; Liu et al., 2012, 2015) with a max thickness 2000 m unconformably cover the Archean basement rocks. From the bottom to the top, it is divided into two parts, the Jiangxian and Zhongtiao Groups. The Jiangxian Group, distributed in the northern part of the Zhongtiao Mountains, consists of a basal meta-conglomerate and quartzite sequence, a middle meta-pelitic schist layer, and a top sequence of potassic bimodal volcanic rocks, erupted between ~2273 and 2161 Ma (Sun et al., 1990, 1992; Zhao, 2006; Zhang, 2012; Liu et al., 2016).

The Zhongtiao Group, distributed in the central section of the Zhongtiao districts, is nearly northeast trending, ~80 km long and 15–8 km wide. This group, unconformably covering the Archean basement rock and the Jiangxian Group, comprises of a sequence of calc-silicates and minor pelitic schist, marble, meta-conglomerate, quartzite, meta-sandstones and minor meta-volcanic rocks and meta-tuffs. The sedimentary sequences (clastic–pelitic-carbonate) deposited in transgression events along the continent marine (Hu and Sun, 1987). The "Hu-Bi type" strata-bound copper deposits are hosted in the graphite schists within this Zhongtiao Group. Sun et al. (1992) reported that the top meta-tuffs erupted in the age of ~2059 Ma through the single zircon evaporation technique. Liu et al. (2012) obtained three youngest detrital zircons with a weighted mean age of 2168 ± 5 Ma from the basal part of the Zhongtiao Group, suggesting this group must have deposited after 2168 Ma. Liu et al. (2015) reported a SHRIMP zircon U—Pb age of ~2086 Ma for an intercalated amphibolite. Therefore, the Zhongtiao Group was deposited in the period between ~2168 and ~2059 Ma.

The Danshanshi Group, distributed in the eastern foothills of Zhongtiao Mountains with a length of ~ 40 km and width of ~2 km, is mainly composed of meta-conglomerates and sandstones. Its maximum depositional age were constrained at 1848 Ma by detrital zircons U—Pb study (Liu et al., 2012). Above these Paleoproterozoic sedimentary sequences are unconformably overlain by Mesoproterozoic unmetamorphosed basaltic andesite, the Xiyanghe Group or Xiong'er Group. The age of these volcanic rocks was defined at 1750 to 1800 Ma, representing the initial formation age of the cover of the North China craton (Zhao et al., 2004).

The Jianxian and Zhongtiao Groups, dominated by quartzite–pelite–carbonate rocks, favor a tectonic setting involving relatively stable sedimentary basin (Sun et al., 1990). These groups underwent a prolonged and complex deformation and metamorphic history. It is debatable whether this mobile belt experienced one-phase or multi-phase metamorphic events, and the precise metamorphic age has not been resolved (Sun et al., 1992; Mei, 1994; Zhao, 2006). Sun et al. (1992) constructed the chronotectonic framework of the Zhongtiao Mountains district and inferred two phase of Zhongtiao Movement at ~1.9 Ga and ~1.85 Ga. The EPMA Th—U—Pb dating of monazite from granitic intrusions in the Sushui complex revealed three age peaks of 1739 Ma, 1850 Ma and 1970 Ma, corresponding to fluid-activation event and metamorphic ages (Liu et al., 2007). These previous geochronogical researches suggested that the study area was likely to undergo a long-lived metamorphism and deformation from 1970 Ma to 1850 Ma, called Zhongtiao Movement (Sun et al., 1990, 1992). The metapelites within the Jiangxian Group are characteristic with the metamorphic mineral assemblages of staurolite, garnet and biotite, recording the peak metamorphic temperature-pressure of 550–600 °C and 5–7 kbar (Mei, 1994). Based on the zoned garnet from the Zhongtiao Group, the peak metamorphic conditions were approximately estimated at 560–580 °C and 3.8–4.5 kbar (Mei, 1994).

3. Deposit geology

The "Hu-Bi type" deposits with a total copper reserve of 0.79 Mt Cu at an average grade of 1.21%, consisting of the Bizigou, Qinjiagou, Tongmugou, Laobaotan and Hujiayu Cu deposits, are located in an approximately 20 km long belt within Zhongtiao Group (Fig. 1b). The Hujiayu Cu deposit, one of the representative "Hu-Bi type" deposits, is mainly hosted in a graphite schist and dolomitic marble, which belong to the upper-middle part of the Zhongtiao Group (Fig. 2a). The orebodies are controlled by an NNE-trending fold and occur as lenticular and stratoid forms in conformity with the host rocks in both limbs of

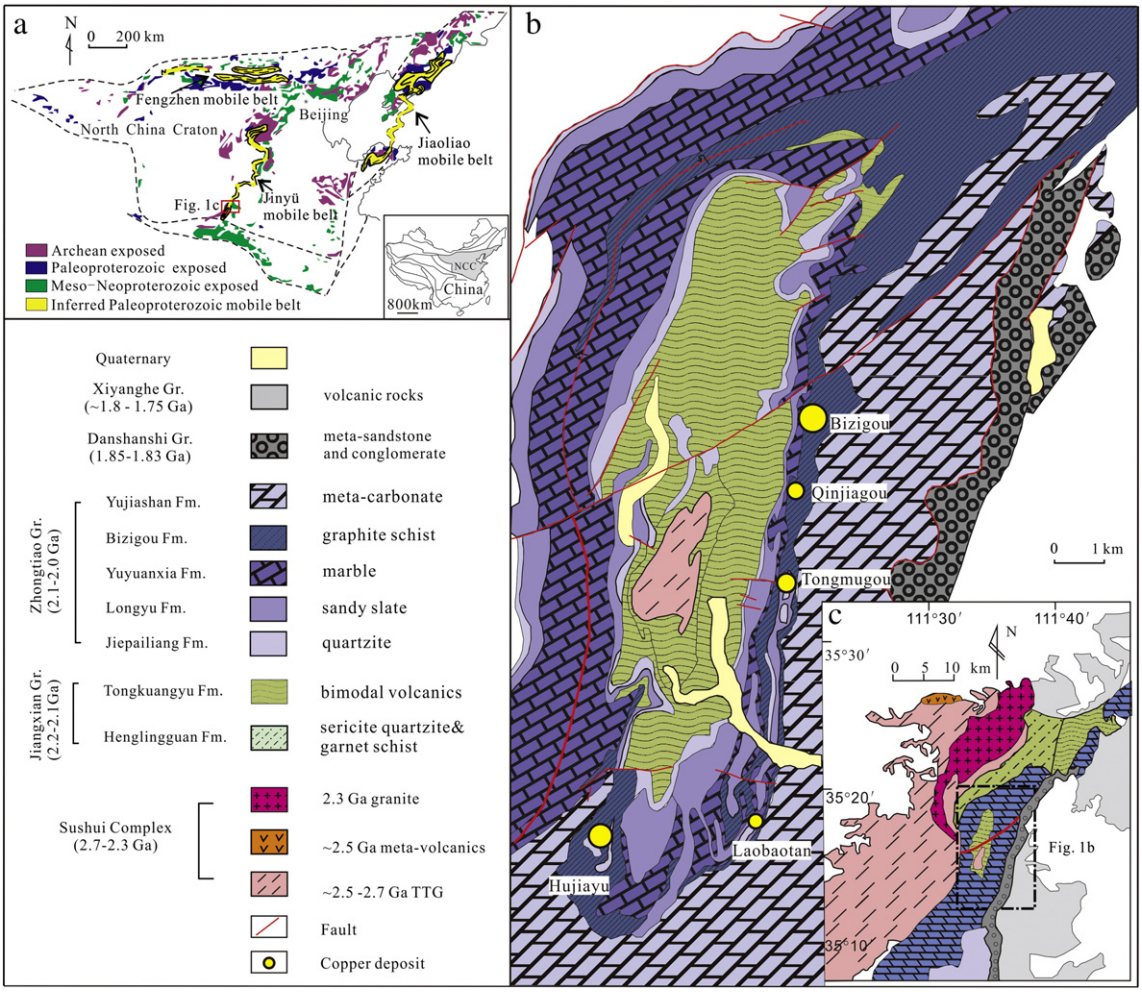

Fig. 1. a. Tectonic location of the study area in North China Craton (modified from Zhai and Peng, 2007; Zhai and Santosh, 2013); b. the regional geological map of Zhongtiao mobile belt showing locations of major "Hu-Bi type" stratabound copper deposits (modified from Sun et al., 1990); c. Simplified geological map of the Zhongtiao Mountains.

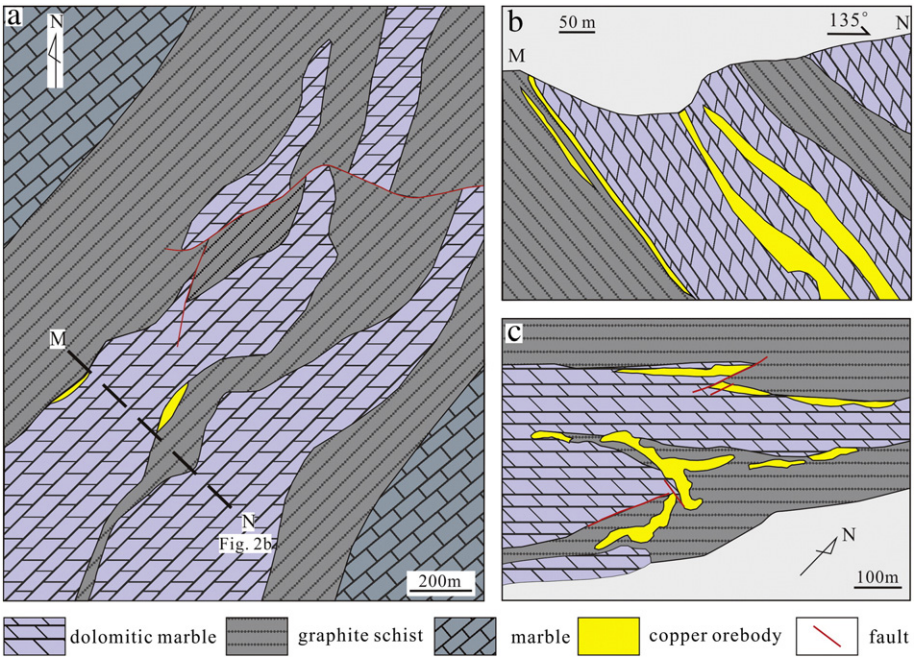

Fig. 2. a. Simplified geological map of the Hujiayu Cu deposit; b. Geological section map showing the host rock and Cu ore-bodies; C. geological plan of No. 5 level underground mine showing the geometry of major ore-bodies. (Modified from WGCGZM, 1978; Hu and Sun, 1987).

the fold (Fig. 2b). At No. 5 level underground mine, the ore-bodies are controlled by interlayer fault zones and become thicker at the core of the fold (Fig. 2c). From field observations and previous study (Hu and Sun, 1987; Jiang et al., 2014), two distinct mineralization stages have been confirmed. The early veinlet-disseminated mineralization stage (stage I) is hosted in graphite schists and parallel to the foliation of the host rock (Fig. 3a). The schist contains quartz, albite, muscovite, dolomite, chlorite, rutile, tourmaline and abundant of graphite. Quartz and albite are concentrated in synmetamorphic veinlets or segregations with minor dolomite and muscovite, while sulfides are also distributed in these veinlets (Fig. 3b). Pyrite is the main sulfide mineral (termed as Py I in Fig. 3b), occurring as scatted subhedral to anhedral grains in quartz–albite–dolomite veinlets (Fig. 3b). Chalcopyrite, with less extensive, coexists with pyrite in veinlets. Graphite probably derived from

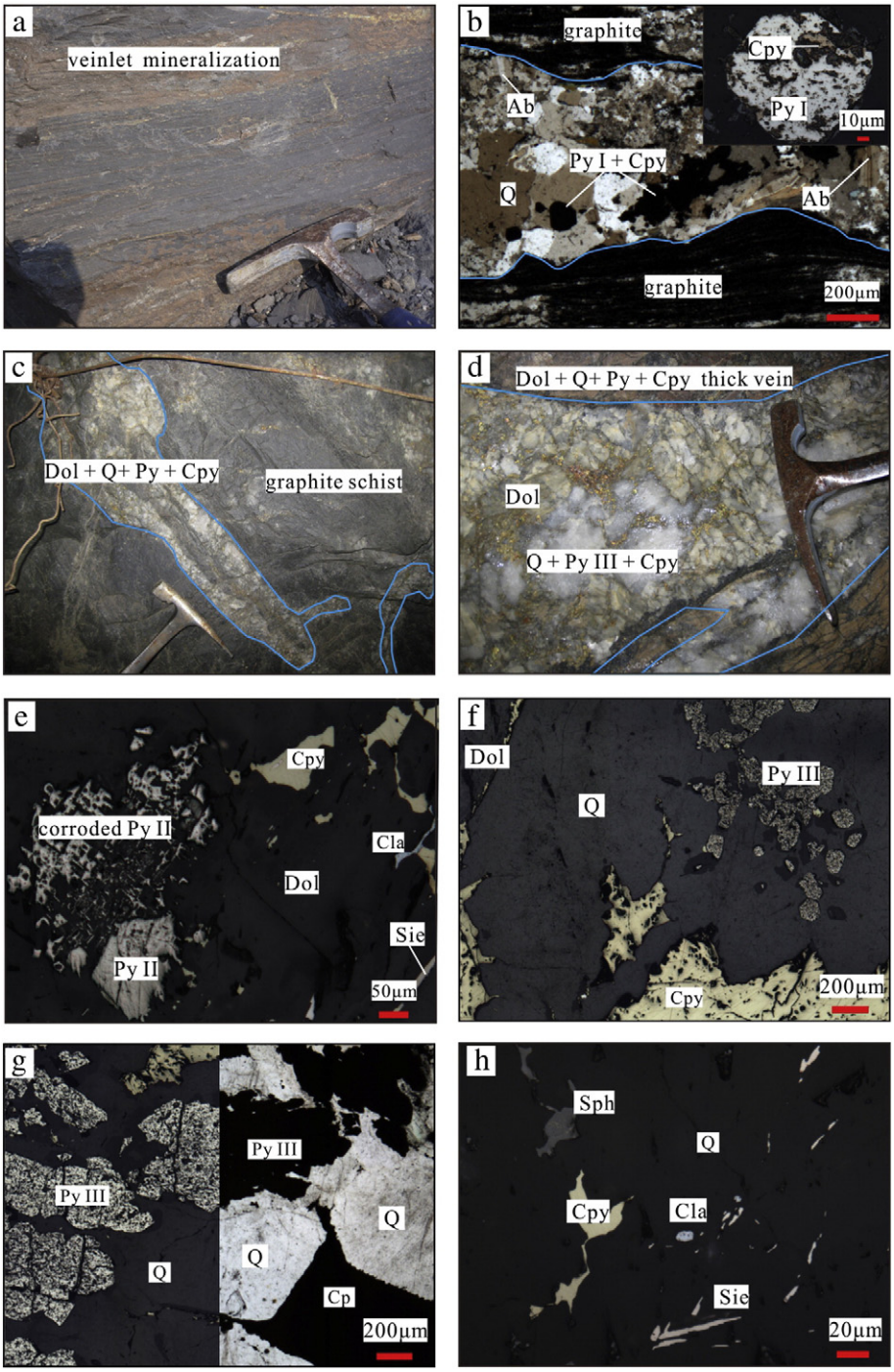

Fig. 3. Photographs of outcrops and mineral assemblages showing two distinct mineralization stages in the Hujiayu Cu deposit. a) The early stage of veinlet-dissenminated mineralization in graphite schist; b) a syn-metamorphic veinlet in graphite schist under cross polarized light showing a pyrite–chalcopyrite–dolomite–quartz–albite assemblage; c) a dolomite–quartz–pyrite–chalcopyrite thick vein in graphite schist; d) the detail of thick vein shows that the major sulfide is intimately associated with a siliceous alteration, which overprints the early hydrothermal dolomitic alteration; e) the Pyrite II, in the hydrothermal dolomite, is characterized by a clear core and corroded mantle with skeletal or porous shapes. This corrosion of Py II was probably triggered by the late siliceous alteration; f) a quartz-pyrite-chalcopyrite mineral assemblage in the gap of hydrothermal dolomite; g) the copper mineralization in thick veins consists of euhedral quartz, pyrite and chalcopyrite (the left side under the reflected light and the right side under cross polarized light); h) a chalcopyrite–clausthalite–siegenite–sphalerite assemblage in the late siliceous stage. Abbreviations: Ab = albite; Q = quartz; Dol = dolomite; Py = pyrite; Cpy = chalcopyrite; Cla = clausthalite; Sie = siegenite; Sph = sphalerite.

organic matter during the prograde metamorphism, is concentrated in narrow zones in parallel to metamorphic segregation veinlets (Fig. 3b). The stage I being synchronous with the metamorphism of the host rocks refers to the syn-metamorphic mineralization. The late stage (stage II) consists of thick and composite dolomite-quartz-sulfide veins, crosscutting the foliation of host rocks (Fig. 3c). Most of copper is associated with siliceous alteration, which overprints the early hydrothermal dolomitic alteration (Fig. 3d). The thick-vein type hydrothermal mineralization stage is subdivided into an early hydrothermal dolomitic alteration stage (stage IIa) and a late siliceous-copper mineralization (stage IIb). The early stage is dominated by dolomite and minor amount of pyrite (termed as Py II in Fig. 3e). The main copper mineralization in this deposit is intimately associated with the late siliceous alteration. Ore minerals mainly comprise chalcopyrite, pyrite (termed as Py III in Fig. 3f, g) with minor sphalerite, siegenite and clausthalite (Fig. 3e, h). Gangue minerals are mainly quartz with less dolomite. Fluid inclusions study of the thick veins showed that the ore-forming fluid belongs to a NaCl—H_2O—CO_2—CH_4 systematics, probably being derived from metamorphic fluids (Qiu et al., 2015).

4. Analytical methods

4.1. Mineral analyses

Electron microprobe analyses (EMPA) of sulfide and selenide minerals were performed on a JEOL JXA-8100 electron microprobe equipped with a BSD detector and an energy dispersive spectrometer (EDS) (Inca Energy 300, Oxford Instruments, UK), at the Institute of Geology and Geophysics, Chinese Academy of Sciences (IGGCAS). For back-scattered electron (BSE) imaging, the voltage was 10–20 keV, and the beam current was adjusted to the voltage (from 0.1 to 10 nA). For EMPA analyses, As, Se, S, Fe, Pb, Co, Bi, Ni, Ag, Cu and Zn were detected in sulfide and selenide minerals using a 20 keV accelerating voltage, 10–20 nA beam current and a 10 s-counting time. Standards used were gallium arsenide for As, guanajuatite for Se, pyrite for S, galena for Pb, guanajuatite for Bi, sphalerite for Zn and native iron, cobalt, nickel, silver and copper for Fe, Co, Ni, Ag and Cu, respectively. The detection limits for the target elements in this study are: As 0.06%, Se 0.03%, S 0.01%, Fe 0.02%, Pb 0.03%, Co 0.02%, Bi 0.05%, Ni 0.02%, Ag 0.02%, Ag 0.04%, Cu 0.02% and Zn 0.03%.

4.2. Laser Raman analysis of graphite

The graphite generally formed in the metasedimentary rocks, deriving from organic matter during the prograde metamorphism. The Raman spectrum of graphite has been widely used as an indication of metamorphic grade (Beyssac et al., 2002; Aoya et al., 2010). The analytical procedures of graphite geothermometry were similar to those reported by Beyssac et al. (2002) and Aoya et al. (2010). In this study, the Raman spectra of graphite were obtained on conventional petrographic thin sections, performed on a HORIBA Jobin Yvon LabRam HR Raman microspectrometer at IGGCAS. The Torus 532 laser with a wavelength of 532 nm and a source power of 44 mW was used in the analysis. Calibration was done using the 520.7 cm^{-1} line of monocrystalline silicon as reference. The graphite was scanned in three 30-second cycles within the spectral range of 1100 to 3500 cm^{-1}. The Raman spectrum of graphite is composed of first-order (1100–1800 cm^{-1}) and second order regions (2500–3500 cm^{-1}). In the first order regions, the spectrum can be decomposed into G band at around 1580 cm^{-1}, D1 band at around 1350 cm^{-1}, D2 band at around 1620 cm^{-1} and D3 band at around 1520 cm^{-1}. These bands can be characterized by parameters such as: peak position (center), peak intensity, peak area (integrated area) and peak width (full width at half maximum). Peak position and peak area were determined using the computer program Peak Fit 4.12 Ver. with a Voigt area function on the assumption that the measured spectrum consists of up to four peaks on a linear baseline (Aoya et al., 2010). The R2 (area ration, D1/(G + D1 + D2)) seems to be best suited to provide quantitative information on temperature(Beyssac et al., 2002). The correlation between R2 ration and the peak metamorphic temperature is well described by the following quardratic equation: T (°C) = $221.0(R2)^2 - 637.1(R2) + 672.3$ (1). This equation works in the temperature range of 330–650 °C with an estimated error of ±50 °C, the coefficient R^2 is 0.96 and R2 values are determined by using a 532-nm laser.

4.3. Sulfur isotope analyses

Sulfur isotopes were determined by MAT-251 mass spectrometer at the Beijing Research Institute of Uranium Geology. Sulfide minerals for isotopic analyses were obtained using heavy liquid separation techniques and were then carefully handpicked under a binocular microscope. Sulfide grains (40–60 mesh) were mixed with cuprous oxide and crushed into 200 mesh powder, SO_2 was produced through the reaction of sulfide and cuprous at 980 °C under a vacuum pressure of 2×10^{-2} Pa. The SO_2 was then measured by MAT-251 mass spectrometer. Results were reported in delta per mil notation with respect to Vienna Canyon Dioblo Troilite (V-CDT). All analytical precisions were better than ±0.2‰.

4.4. Chalcopyrite Re—Os dating

Chalcopyrites for Re—Os dating were separated from chalcopyrite-bearing thick veins (stage II), collected from underground tunnels (Level 240 m) at Hujiayu. All chalcopyrites were carefully hand-picked under binocular microscope to devoid weathering or oxidation.

Re—Os isotopes analyses were performed at the State Key Lab of Ore Deposit Geochemistry, Institute of Geochemistry, and Chinese Academy of Sciences. A detailed description of the Re—Os isotopes analytical procedure is available in Qi et al. (2010). Briefly, 3 g of chalcopyrite separates were first digested with HNO_3 in a 120 ml Carius tube. The released additional gas and a small portion of volatile Os (~6% of total Os) were collected by 2 ml of 10 mol L^{-1} HCl in a glass tube cooled with an ice-water bath. After samples were completely reacted with HNO_3, the HCl solution containing all the released Os was transferred back to the Carius tube, which was then cooled in an ice-water bath, 20 ml of cooled HNO_3 and appropriate volumes of weighted ^{185}Re and ^{190}Os spikes were added. The Carius tube was sealed using an oxygen-methane torch and then heated to 200 °C for about 10 h. Os was separated from the matrix by distillation and Re was separated from the remaining solution using anion exchange resin technique.

Re and Os isotopes were measured using an ELAN DRC-e ICP-MS at same institute. Iridium was added to Re and Os bearing solution for mass discrimination correction, following calibration method described by Schoenberg et al. (2000). In order to give the highest intensity of Os, the volume of the Os solution for ICP-MS measurement should be reduced as small as possible and Os should be oxidized to its highest valence. Measured ^{187}Os and ^{192}Os were referred to the spike isotope ^{190}Os and were used to determine radiogenic ^{187}Os and common Os concentrations in each sample. The results were reported at 1 σ level. Total blanks of Re and Os were 6.4 pg and 2.0 pg, respectively. The low blank level and detection limits ensured the accuracy of the determination of low Re and Os concentrations. The isochron was calculated by the ^{187}Re decay constant of 1.666×10^{-11}/year (Smoliar et al., 1996) using the ISOPLOT program of Ludwig (2003).

Although there is no chalcopyrite reference material for Re—Os dating, the molybdenite standard JDC (molybdenite from the Jinduicheng ore deposit) was dated as an unknown sample and yielded a model age of 138.7 ± 2.1 Ma, which is in good agreement with the recommended value of 139.6 ± 3.8 Ma (Du et al., 2004). Chalcopyrite and molybdenite are both sulfide minerals, and hence can be used to evaluate the accuracy of the analyses (Huang et al., 2015; Ding et al., 2016). Ding et al. (2016) obtained a reliable pyrite Re—Os age using a

molybdenite standard. Thus, chalcopyrite Re—Os age in this study is also reliable.

5. Analytical results

5.1. Graphite geothermometry

The early stage of mineralization formed synchronously with peak metamorphism and the sulfide minerals occurred in the metamorphic segregation veinlets. These veinlets were surrounded by graphite. As discussed above, the graphite is a good temperature proxy and records the highest temperature that the host rocks had undergone. In this study, the representative Raman spectrum of graphite in the first-order region shown in Fig. 4 and the relevant parameters of the decomposition spectra are summarized in Table 1. After calculations, the peak area ratio R2 is at the average of 0.23 ± 0.07 (1 σ, n = 19). Based on the graphite thermometer equation (1), we obtain the temperature of 546 ± 35 °C (1 σ, n = 19), representing the peak metamorphic temperature.

5.2. Mineral compositions

5.2.1. Pyrite paragenesis

Pyrite occurred in all stages of the Hujiayu Cu deposit, showing a wide range of habits and paragenetic arrangements. Three generations of pyrite can be distinguished based on detailed petrographic observation and geochemical characters. EPMA analyses of the various generations of pyrite are summarized in Table 2.

Pyrite I commonly occurs as euhedral to subhedral disseminated grains in the graphite schist (Figs. 3b; 5a). Based on the EPMA analysis, trace element (e.g. Co, Ni, and As) contents in pyrite I are below the detection limit. The limited valid data shows that the Co/Ni ratios are in highly variable ranging from 6.87 to 0.26 with an average value of 1.91.

Pyrite II is associated with the early hydrothermal dolomitic alteration during the vein type mineralization. It occurs in dolomite-rich veins and was commonly corroded into porous pyrite by the late stage of copper-bearing fluids (Fig. 5b–c). Some pyrite II is characterized by the special rim-core texture, consisting of a clear core and corroded rim with skeletal or porous shapes (Fig. 5b). As revealed by the EPMA results, the clear core has high cobalt content, with a range of 2.66 to 7.08 wt.%. The corroded rim is free of trace elements close to pure pyrite composition. It may have been the product of the late stage fluid modification. Obviously, the EPMA results of the corroded part cannot represent the composition of pyrite II. Due to the high contents of cobalt, the Co/Ni ratios of pyrite II are varying from 100 to 737 with an average of 279. It is notable that the accuracy of the Co/Ni ration is highly depended on the precision of nickel content.

Pyrite III occurs in the quartz veins, associated with chalcopyrite, siegenite. Pyrite III displays three main forms in the quartz veins: (1) as mineral inclusion in quartz; (2) as cracked pyrite with infillings of quartz and chalcopyrite in its micro-fissures; (3) rims around chalcopyrite or occurs inside chalcopyrite. Although the pyrite III is distributed in varied forms, no obvious difference from the EPMA results. The cobalt and nickel contents are below the detection limit.

5.2.2. Clausthalite–siegenite–sphalerite–chalcopyrite assemblages

A clausthalite–siegenite–sphalerite–chalcopyrite mineral assemblage was observed in stage IIb, distributed in the rim of dolomite crystal in the dolomite-quartz-sulfide thick veins (Fig. 3e) and quartz-sulfide veins (Fig. 3h). Clausthalite, a lead selenide, was observed exclusively in dolomite (Fig. 3e) and was associated with siegenite as subhedral crystal of up to 30 to 20 μm in size (Fig. 3h). According to EPMA analyses (Table 3), the clausthalite is PbSe—PbS solid-solution series, covering the range $Pb_{0.93}(S_{0.39}Se_{0.60})$—$Pb_{0.98}(S_{0.83}Se_{0.17})$. The PbSe—PbS series can be completely miscible in nature (Förster, 2005), however, the clausthalite do not cover the entire series in this study (Fig. 6a).

Siegenite, a rare thiospinel with the chemical formula $(Co, Ni)_3S_4$, was confirmed by SEM-EDS analysis. In the dolomite-quartz-sulfide veins, siegenite is a common phase occurring as acicular crystals up to 10 to 30 μm in length (Fig. 3h) in dolomite or quartz. In this study, siegenite has a range in chemical composition (Table 4) that overlaps with previously reported siegenite occurrences worldwide (Craig et al., 1979; White et al., 2014). The Co—Ni scatter plot shows two distinct groups of siegenite (Fig. 6b). The siegenite in the rim of the dolomite has almost identical content in Co and Ni, with the formulae $(Co_{1.06–1.59}Ni_{1.19–1.27}Fe_{0.19–0.55}Cu_{0.00–0.25})S_4$, while the grains in quartz veins contain more Co than Ni, with the formulae $(Co_{1.74–2.07}Ni_{0.09–0.16}Fe_{0.07–0.11}Cu_{0.00–0.06})S_4$.

The sphalerite in this assemblage occurs with chalcopyrite blebs (Fig. 3h), termed as “chalcopyrite disease” by Barton and Bethke (1987) to describe the sphalerite-chalcopyrite relationship. The chalcopyrite disease is commonly interpreted as the result of Cu diffusion through sphalerite, sphalerite replacement, or chalcopyrite co-precipitation (Barton and Bethke, 1987; Bortnikov et al., 1991). Based on EPMA results (Table 5), we find that most sphalerite is poor in Fe and Cu and locates close to the region of Fe—Zn substitution tendency (Fig. 6c). One sphalerite with elevated Cu content is located in the

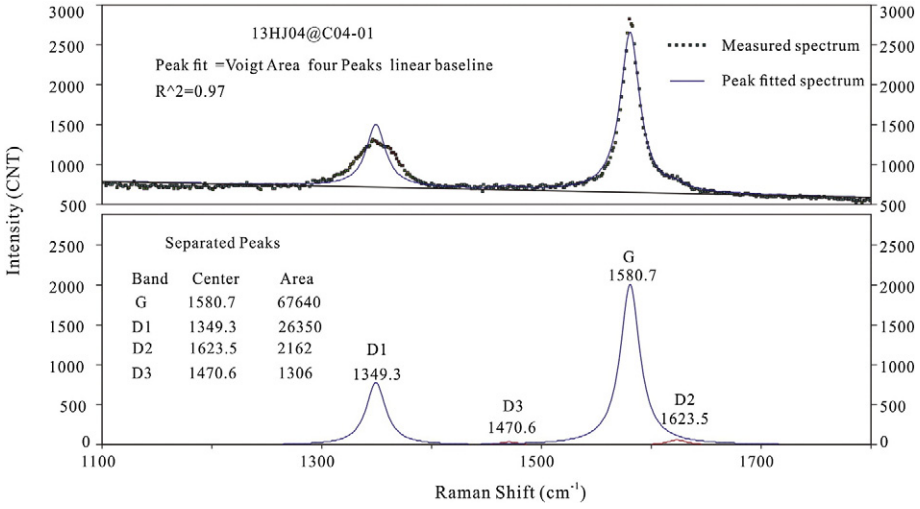

Fig. 4. Representative of decomposition of the first-order region (1100–1800 cm^{-1}) of the Raman spectrum of graphite (C04-01 analysis spot of 13HJ04 sample) using the computer program Peak Fit software.

Table 1
Parameters obtained from the decomposition of the Raman spectra of graphite from the graphite schist in the Hujiayu copper deposit and the estimated temperature of analyzed spots.

Analysis spot no.	D1		G		D2		R2	T(°C)
	Center	Area	Center	Area	Center	Area		
13HJ14@C01-1	1355.5	8915	1580.5	57,010	1620.7	4838	0.13	596
13HJ14@C01-2	1355.4	20,130	1580.8	53,080	1621.1	5294	0.26	523
13HJ14@C01-3	1355.8	20,600	1581.4	105,400	1621.5	4141	0.16	577
13HJ14@C01-4	1345.0	35,120	1582.0	191,600	1496.1	14570	0.15	584
13HJ14@C01-5	1358.1	8657	1582.8	51,570	1623.3	532	0.14	586
13HJ14@C01-6	1357.8	9300	1582.3	58,550	1622.8	640	0.14	590
13HJ14@C02-1	1353.5	25,220	1582.1	86,120	1623.9	974	0.22	540
13HJ14@C02-2	1353.5	25,300	1582.1	86,280	1623.8	962	0.22	540
13HJ14@C02-3	1352.1	10,680	1582.1	30,440	1650.9	312	0.26	523
13HJ04@C01-1	1350.2	11,190	1582.1	22,710	1671.7	13	0.33	486
13HJ04@C01-2	1351.3	8810	1581.7	23,230	1622.1	651	0.27	517
13HJ04@C01-3	1349.8	4998	1581.2	22,290	1617.2	427	0.18	565
13HJ04@C01-4	1349.4	4448	1581.0	10,110	1621.3	477	0.30	503
13HJ04@C02-1	1350.4	10,480	1580.9	47,830	1620.0	1212	0.18	567
13HJ04@C03-1	1351.1	12,060	1580.8	29,630	1617.0	2602	0.27	515
13HJ04@C04-1	1349.3	26,350	1580.7	67,640	1623.5	2162	0.27	514
13HJ04@C05-1	1356.9	6288	1580.5	25,910	1621.7	759	0.19	559
13HJ04@C05-2	1355.8	20,420	1581.4	103,000	1621.1	4408	0.16	576
13HJ04@C05-3	1349.4	4448	1581.0	101,10	1621.3	477	0.30	503
Average	1352.7	14,390	1581.4	56,974	1619.0	2392	0.22	546
Standard Deviation	3.6	8923	0.7	44,011	32.5	3406	0.06	35

Note: 13HJ04 and 13HJ14 are the sample of graphite schist hosted copper orebodies. Peak position (center) and peak area were determined using the computer program Peak Fit 4.12 Ver. The R2 value is the ratio of D1 peak area to the total G, D1 and D2 peak area, expressed as D1/(G + D1 + D2). The temperature (T) is calculated by the following quadratic equation: $T\,(°C) = 221.0 * (R2)^2 - 637.1 * (R2) + 672.3$.

'chalcopyrite disease' region, suggesting this sphalerite was polluted and cannot reflect the initial composition. Keith et al. (2014) proposed that sphalerite from the sediment-starved vent sites is applicable to estimate minimum fluid temperatures of sphalerite precipitation at hydrothermal systems. The sphalerite in this study shares a similar composition with the sphalerite from the sediment-starved vent sites indicating they form at uniform conditions (Fig. 6d), so it can be used to estimate the precipitation temperature of sphalerite. The average temperature of 256 ± 9 °C (1σ, n = 7) is calculated basing on the equation — Fe/Zn (sphalerite) = 0.0013*T-0.2953 (Keith et al., 2014).

5.3. Sulfur isotopic composition

In this study, the sulfur isotope analyses were performed on the early stage of disseminated-veinlet mineralization (stage I) and the late stage of thick vein mineralization (stage II). The results are shown in Table 6. Pyrite collected from the stage I has the $\delta^{34}S$ values from 10.1 to 19.7‰. Chalcopyrite and pyrite from the stage II have similar $\delta^{34}S$ values, ranging from 12.9 to 19.2‰, and 17.5 to 19‰, respectively. Combining with the previous sulfur isotopic analyses of sulfide from the Hujiayu Cu deposit (WGCGZM, 1978), we present the frequency histogram showing $\delta^{34}S$ values distribution in Fig. 7.

5.4. Chalcopyrite Re—Os age

Results of chalcopyrite Re—Os dating are listed in Table 7. Chalcopyrite from the Hujiayu Cu deposit contains 5.26 to 14.43 ppb Re, 0.0033 to 0.0046 ppb common Os, 3.29 to 9.04 ppb ^{187}Re, and 0.108 to 0.321 ppb ^{187}Os, respectively. $^{187}Re/^{188}Os$ values vary between 6531 and 19204, and $^{187}Os/^{188}Os$ ratios range from 212 to 641. The total common Os (0.0033–0.0046 ppb) is less than half of the calculated radiogenic ^{187}Os. Stein et al. (2000) proposed the concept of Low-Level Highly Radiogenic (LLHR) sulfides which describes sulfide with high concentrations of Re and Os dominated by radiogenic ^{187}Os, and the $^{187}Re/^{188}Os$ ratio is over 5000. Using traditional $^{187}Re/^{188}Os$ versus $^{187}Os/^{188}Os$ plots for LLHR sulfide samples introduces large analytical uncertainties and highly corrected errors as ^{188}Os is poorly determined. Thus, the relatively well determined ^{187}Re and ^{187}Os data should be best plotted in the ^{187}Re versus ^{187}Os diagram to obtain precise age. Since our data fit the LLHR classification, precise ages are routinely calculated directly from the ^{187}Re and ^{187}Os data (Stein et al., 2000).

Regression of total six chalcopyrite samples in ^{187}Re—^{187}Os diagram yields an isochron age of 2118 ± 310 Ma with a MSWD of 6.0 (Fig. 8a). The large MSWD value (the mean square of weighted deviation) of the isochron indicates this isochron age is of doubtful reliability. Two samples show scatter above (13HJ28) or below (13HJ32) the isochron, making it difficult to obtain precise age (Fig. 8a). One plausible explanation is that Re—Os isotopes in these two samples show open-system behavior through the process of Re gain or Os diffusion due to hydrothermal or supergene alteration (Lambert et al., 1998; Morelli et al., 2004; Huang et al., 2015; Ding et al., 2016). Additionally, they have very high Re/Os ratios, therefore, even a small amount of open systems behavior could have a large influence on the age (Gregory et al., 2008). Thus, these two samples are removed from the data and the remaining four samples define an ^{187}Re—^{187}Os isochron age with an age of 1938 ± 140 Ma (1 σ) and a MSWD of 0.81 (Fig. 8b). High $^{187}Re/^{188}Os$ ratios (>5000) in remaining four chalcopyrite samples allow us to calculate single mineral model age, yielding a weighted age of 1952 ± 39 Ma (1 σ) with a MSWD of 1.5 (Fig. 8c). This result is consistent with the isochron age within error, demonstrating that the weighted mineral model age of 1952 ± 39 Ma reported here is also reliable and geologically meaningful.

6. Discussion

6.1. Evolution of ore-forming processes

Based on field and petrographic observations, we delineated the evolution of the ore-forming process and constrained the physicochemical conditions of the hydrothermal fluids in the Hujiayu Cu deposit.

6.1.1. Syn-metamorphic stage

The syn-metamorphic stage is referred to the period close to peak metamorphism of the host rocks. During the metamorphic process, the sedimentary rocks were metamorphosed into graphite schist, which consist of quartz–albite–carbonate metamorphic veinlets, disseminated pyrite and chalcopyrite within veinlets and the surrounding graphite (Fig. 3a–b). Graphite geothermometry indicated that the

Table 2
Representative EPMA data of various generations of pyrite in the Hujiayu copper deposit.

No.	Py paragenesis	S	Fe	Se	Pb	Co	Ni	Total	Co/Ni
Mass percent (wt.%)									
1	Pyrite I	53.14	46.94	0.01	0.30	0.10	0.015	100.51	6.87
2	Pyrite I	53.92	47.26	0	0.27	0	0	101.45	NULL
3	Pyrite I	53.42	47.10	0	0.26	0	0.01	100.79	0.00
4	Pyrite I	52.96	46.76	0	0.36	0	0.02	100.10	0.00
5	Pyrite I	53.41	46.89	0.02	0.27	0	0.03	100.61	0.00
6	Pyrite I	50.60	44.36	0.04	0.30	0.05	0.03	95.39	1.41
7	Pyrite I	53.08	46.65	0	0.28	0	0.06	100.07	0.00
8	Pyrite I	51.37	45.78	0	0.32	0.116	0.34	97.93	0.34
9	Pyrite I	53.50	47.82	0	0.33	0	0.00	101.65	0.00
10	Pyrite I	53.72	47.22	0.01	0.26	0	0	101.20	NULL
11	Pyrite I	52.94	46.95	0.01	0.29	0.05	0.20	100.45	0.26
12	Pyrite I	52.68	46.59	0	0.38	0.09	0.07	99.80	1.32
13	Pyrite I	50.67	44.32	0	0.262	0.28	0.06	95.58	5.00
14	Pyrite I	53.53	46.67	0.08	0.36	0.16	0.16	100.97	1.00
15	Pyrite I	53.00	46.98	0.03	0.31	0.04	0.11	100.47	0.36
16	Pyrite I	52.63	46.90	0	0.28	0.06	0.1	99.97	0.64
	average	52.78	46.57	0.01	0.30	0.06	0.08	99.81	1.91
17	Pyrite II	53.06	40.53	0.10	0.26	6.38	0.02	100.35	319.05
18	Pyrite II	53.38	40.55		0.19	6.19	0.02	100.33	306.49
19	Pyrite II	53.95	40.06	0.02	0.31	6.72	0.06	101.12	117.84
20	Pyrite II	52.80	39.53	0	0.44	7.08	0.07	99.92	99.72
21	Pyrite II	53.22	40.12		0.32	6.55	0.03	100.25	191.64
22	Pyrite II	53.42	40.43		0.26	6.22	0.03	100.37	182.94
23	Pyrite II	53.57	43.20	0	0.32	4.11	0	101.19	NULL
24	Pyrite II	52.54	43.81	0	0.25	3.17	0	99.77	NULL
25	Pyrite II	53.51	44.22	0	0.30	2.95	0.004	100.98	737.25
26	Pyrite II	53.17	44.57	0	0.29	2.66	0	100.68	NULL
	average	53.26	41.70	0.02	0.29	5.20	0.02	100.50	279.27
27	Pyrite III	53.44	46.18	0	0.32	0	0.09	100.03	0
28	Pyrite III	53.64	46.25	0	0.31	0	0.04	100.24	0
29	Pyrite III	52.95	46.15	0	0.40	0	0.03	99.53	0
30	Pyrite III	53.72	46.04	0	0.33	0	0	100.08	NULL
31	Pyrite III	54.31	45.14	0.05	0.37	0	0.03	99.89	0.0
32	Pyrite III	52.78	44.96	0	0.32	0	0	98.06	NULL
33	Pyrite III	54.15	46.52	0.03	0.21	0	0.02	101.00	0.00
34	Pyrite III	53.61	45.95	0	0.43	0	0	99.992	NULL
35	Pyrite III	53.27	45.90	0	0.32	0	0	99.539	NULL
36	Pyrite III	52.80	45.32	0.04	0.27	0	0.02	98.472	0.00
37	Pyrite III	53.61	45.81	0	0.25	0	0.01	99.721	0.00
38	Pyrite III	54.01	46.38	0.01	0.29	0	0	100.72	NULL
39	Pyrite III	53.15	45.68	0.01	0.24	0.04	0.01	99.16	6.00
40	Pyrite III	53.72	45.95	0	0.20	0.09	0.07	100.05	1.27
	average	53.51	45.87	0.01	0.30	0.01	0.02	99.75	3.64

Note: If the Ni content is zero, the Co/Ni ratio cannot be calculated. Therefore, the ratio is NULL.

highest temperature the graphite schist host rocks had undergone was ca. 546 °C. At such high temperature, the primary mineral assemblages and original textural characters in the sedimentary rocks cannot retain anymore and some sulfide minerals may remobilize and re-precipitate (Wen et al., 1996; Tomkins, 2010).

At this stage, pyrite I is the dominant sulfide mineral with less chalcopyrite. It is interpreted to have developed during metamorphic processes. The Co/Ni ratio in pyrite was considered as an empirical indicator of pyrite genesis in previously studies (Roberts, 1982; Bajwah et al., 1987; Craig et al., 1998; Clark et al., 2004). Comprehensive reviews indicate that the hydrothermal pyrite generally has Co/Ni ratio >1, while the sedimentary pyrite has Co/Ni ratio <1. However, the cobalt and nickel contents of pyrite I are extremely low and the Co/Ni ratios are variable (plotted above or below the line of Co/Ni = 1 in Fig. 5f). This indicates that pyrite I was probably derived from the sedimentary pyrite with Co/Ni ratio <1. The sulfur fugacity is calculated at −4.8, assuming the formation of pyrite at the temperature of 500 °C.

6.1.2. Hydrothermal copper mineralization stage

The hydrothermal mineralization stage (stage II) was characterized by the dolomite-quartz-sulfide composite veins (Fig. 3c-d), subdivided into the early hydrothermal dolomitic alteration stage (IIa) and the late siliceous-copper mineralization stage (IIb).

During the stage IIa, the pyrite II accompanied by hydrothermal dolomite has Co/Ni ratios higher than 100, which are thought to be of hydrothermal origin, and has the high cobalt contents ranging from 2.66 to 7.08 wt.%, which can be termed as cobaltiferous pyrite. The cobaltiferous pyrite is a kind of FeS_2—CoS_2 solid solutions with the high cobalt content, approximately higher than 3 wt.% (Klemm, 1965; Brown and Bartholomé, 1972; Hem and Makovicky, 2004). The cobaltiferous pyrite can also be found in the various Cu—Co deposits, e.g. the Central African copper belt where Proterozoic sedimentary rocks contain stratiform copper–cobalt orebodies over a distance of more than 500 km (e.g. Brown and Bartholomé, 1972; Cailteux et al., 2005), the Idaho cobalt belt which consists of strata-bound copper–cobalt deposits hosted in Proterozoic metasedimentary rocks (Nold, 1990; Slack, 2012), and the Prince Lyell copper deposit, western Tasmania, Australia, where orebodies are hosted in the Cambrian volcanic rocks overprinting the late Devonian deformation (Raymond, 1996). Previous studies have reported the cobaltiferous pyrite in the "Hu-Bi type" strata-bound copper deposits with the cobalt content ranging from 3.10 to 13.73 wt.% (e.g. Shi and Li, 2000). They suggested the cobaltiferous pyrite was precipitated from cobalt-rich hydrothermal fluids (e.g. Shi and Li, 2000). However, factors controlling the precipitation of cobaltiferous pyrite in the hydrothermal conditions are still obscure and the cobalt–iron ration in aqueous solutions in equilibrium with cobaltiferous pyrite is not yet well known (Bartholomé et al., 1971; Hem and Makovicky, 2004). The solvus reported by Klemm (1965) in the system CoS_2—NiS_2—FeS_2 at temperature of 700 to 300 °C has been used as a geothermometric indicator (e.g. Brown and Bartholomé, 1972; Fanlo et al., 2004). According to the experimental results of Klemm (1965), the cobaltiferous pyrite presented here was precipitated from the hydrothermal fluids approximately at the temperature range of 400 to 300 °C.

Stage IIb resulted in the main chalcopyrite precipitation accompanying the intense siliceous alteration. Pyrite III in this stage has cobalt contents near the detection limit. Given that the cobaliferous pyrite was observed in the stage IIa accompanying with hydrothermal dolomite, it is inferred that cobalt prefers to form siegenite at low temperature, whereas it is incorporated into pyrite structure at high temperature. This stage of copper mineralization contains Co-Ni bearing sulfide and Pb-bearing selenide, which are sensitive indicators of S_2(gas) and Se_2(gas) fugacity. In this study, we mainly focused on this mineral assemblage to determine the chemical condition during vein formation and copper mineralization process. Fugacity–Fugacity diagrams can be used to predict the equilibrium assemblages for a given system, to estimate the prevailing $f(Se_2)$ and $f(S_2)$ during mineral deposition or re-equilibration and to evaluate the evolution of $f(Se_2)$ and $f(S_2)$ with time in deposits (Simon et al., 1997). When constructing fugacity diagrams, the oxygen fugacity and temperature must be specified. (1) From the mineral assemblages study, the lack of magnetite or hematite indicates a low oxygen fugacity; (2) previous fluid inclusion study suggested that copper mineralization occurred at the temperature of 203–230 °C (Qiu et al., 2015); 3) sphalerite in this mineral assemblage suggests that the fluid temperature is around 256 °C. Thus, the fugacity–fugacity diagram used here is constructed at 250 °C. The method and thermodynamic data to construct the diagram were taken from Simon and Essene (1996); Nekrasov (1996) and Xu et al. (2014). A log $f(S_2)$–log $f(Se_2)$ diagram is constructed to constrain the chemical conditions of the ore-forming fluids at the copper mineralization (Fig. 9).

The upper limit S_2 (gas) fugacity is constrained from the stability of siegiente by the following reaction: $Co_3S_4 + S_2 = 3\ CoS_2$. The lower limit S_2 fugacity is inferred from the chalcopyrite stable field, calculated from the (bonite + pyrrhotite)-chalcopyrite equilibrium. The S_2

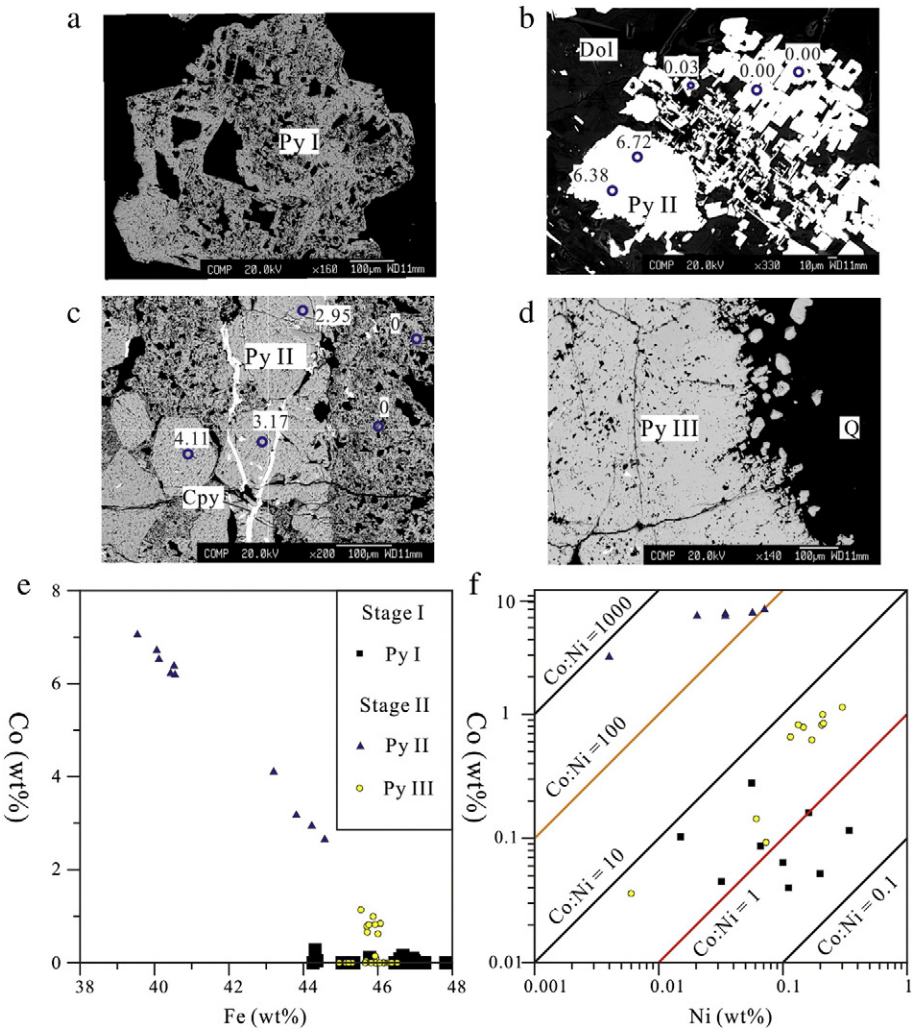

Fig. 5. The cobalt and nickel content in various generations of pyrite in the Hujiayu Cu deposit based on EPMA data (e–f). a. Py I in the graphite schist; b. Py II hosted in the dolomitized of marble, numbered circles representing the cobalt content; c. Py II in the dolomite–rich veins, being corroded by the late stage of copper bearing fluid; d. showing Py III in the copper bearing quartz veins; e. Co-variation of Co and Fe in various generations pyrite. Co/Ni ratios distribution diagram for various generations pyrite.

fugacity of this stage is ranging from −18.7 to −11.7. The occurrence of clausthalite restrains the Se_2 fugacity on the line of log f(Se_2) = log f(S_2) − 3.

According the S_2 and Se_2 fugacity calculations above, it is inferred that the sulfur fugacity is relatively high at stage I and stage IIa, while stage IIb is marked by the a drop in sulfur fugacity and a strong increase in selenium fugacity after the major chalcopyrite precipitation.

6.2. Timing of copper mineralization

The timing of copper mineralization of the "Hu-Bi type" copper deposit in the Zhongtiao Mountains district has long been controversial, largely due to the lack of an acceptable mineralization age. Tao (1985) dated uraninite and brannerite from the Bizigou Cu deposit, obtaining a U—Pb upper intercept age of ~1830 Ma. They found these uranium-

Table 3
EPMA analysis of clausthalite from the Hujiayu copper deposit.

No.	As	Se	S	Fe	Pb	Co	Bi	Ni	Cu	Zn	Total	Formula
Mass percent (wt. %)												
1	<0.04	13.38	7.12	0.44	78.49	<0.02	<0.05	<0.02	0.45	<0.02	99.87	$Pb_{0.96}(S_{0.57}Se_{0.43})$
2	<0.04	15.92	5.48	0.32	74.63	<0.02	<0.05	<0.02	<0.02	<0.02	96.35	$Pb_{0.98}(S_{0.57}Se_{0.55})$
3	<0.04	13.49	7.06	0.29	78.50	<0.02	<0.05	<0.02	<0.02	2.01	101.34	$Pb_{0.94}(S_{0.55}Se_{0.42})$
4	<0.04	14.82	6.04	0.38	77.28	0.126	<0.05	0.107	<0.02	<0.02	98.76	$Pb_{0.98}(S_{0.50}Se_{0.49})$
5	<0.04	13.16	6.60	0.22	76.44	<0.02	<0.05	<0.02	<0.02	1.00	97.42	$Pb_{0.97}(S_{0.54}Se_{0.44})$
6	<0.04	8.99	8.89	0.33	79.97	<0.02	<0.05	<0.02	<0.02	0.49	98.67	$Pb_{0.98}(S_{0.70}Se_{0.29})$
7	<0.04	13.34	7.44	0.81	78.05	<0.02	<0.05	<0.02	0.95	<0.02	100.59	$Pb_{0.93}(S_{0.57}Se_{0.42})$
8	<0.04	14.04	6.35	0.03	77.41	<0.02	<0.05	<0.02	<0.02	<0.02	97.83	$Pb_{1.00}(S_{0.53}Se_{0.47})$
9	<0.04	14.53	6.65	0.08	79.64	<0.02	<0.05	<0.02	<0.02	<0.02	100.89	$Pb_{0.99}(S_{0.53}Se_{0.47})$
10	<0.04	5.33	10.79	0.21	82.55	<0.02	<0.05	<0.02	<0.02	0.26	99.14	$Pb_{0.98}(S_{0.83}Se_{0.17})$
11	<0.04	18.49	4.93	0.70	76.16	<0.02	<0.05	<0.02	1.18	<0.02	101.46	$Pb_{0.93}(S_{0.39}Se_{0.60})$

Formula recalculated based on two atoms.

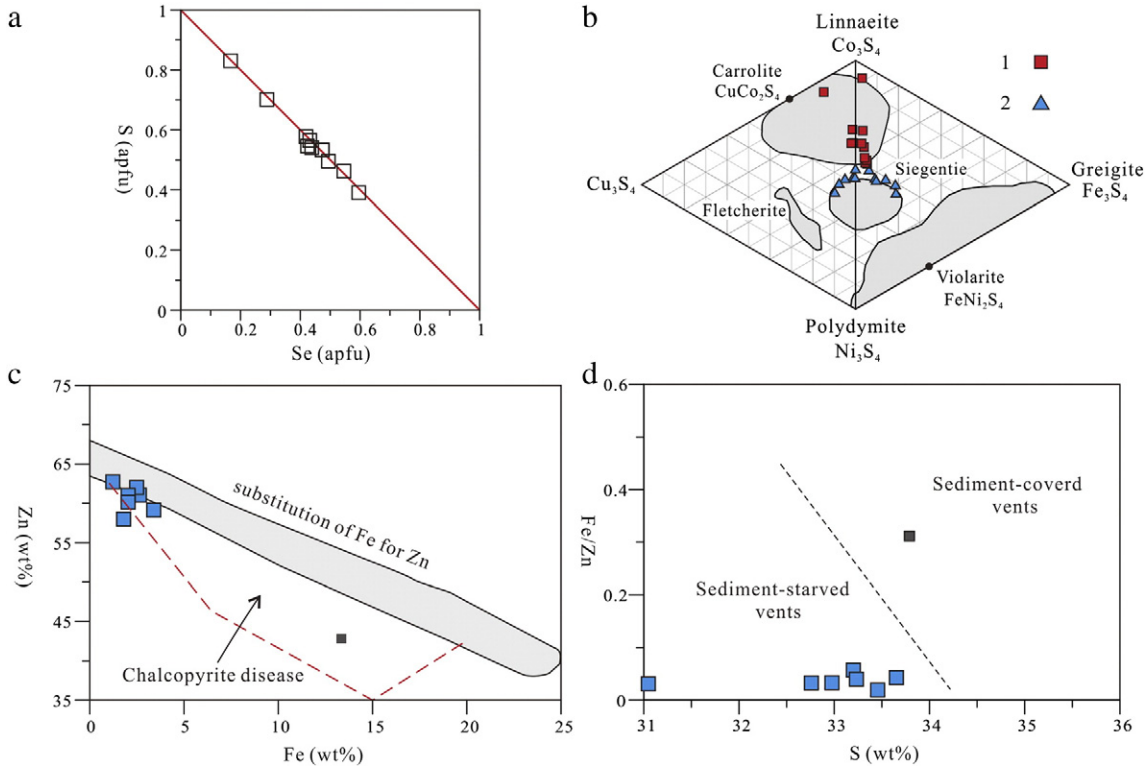

Fig. 6. a) Extent of miscibility in the natural clausthalite-galena series from the Hujiayu deposit in terms of atoms-per-formula-unit of S vs Se. b) Siegenite composition from the Hujiayu deposit plotted in the Co—Ni—Cu—S and Co—Ni—Fe—S ternary corresponding to the formulae. The shaded areas show the approximate range of thiospinel composition obtained from Craig et al. (1979). 1—siegenite in the rim of the dolomite; 2—siegenite as mineral inclusion in quartz and chalcopyrite. c) Fe versus Zn in sphalerite showing the region of chalcopyrite disease. The shade region stands for the tendency of a substitution of Fe for Zn (Keith et al., 2014). The dashed line represents the extent of chalcopyrite disease (Keith et al., 2014). d) Sulfur versus Fe/Zn in sphalerite from the Hujiayu deposit; the dashed line separates the distinct compositions between sphalerite from sediment-hosted sites and the one form the sediment-starved sites (Keith et al., 2014).The black square in c and d represents the polluted sphalerite and see details in text.

bearing minerals were associated with the copper-rich veins and suggested this age represented the timing of copper mineralization. However, the high U content of dated minerals may lower the U—Pb age, and the U—Pb system of uraninite also may be disturbed by the thermal event during ~1800 to 1750 Ma volcanic eruptions. It is not widely accepted that copper mineralization occurred at ~1830 Ma. Recently, Zhang et al. (2013a) reported a molybdenite Re—Os isotopic model age of 1901 ± 24 Ma. The analyzed molybdenite was collected from sulfide quartz veins, which distributed in the cross fractures and the interlayer fracture zones (Zhang et al., 2013a). Obviously, this age constrained the time of molybdenum mineralization stage in the "Hu-Bi" type copper deposits and was close to the timing of copper mineralization.

In this study, chalcopyrite from the copper-rich quartz veins in the Hujiayu Cu deposit was dated by Re—Os isotopic method for the first time, yielding a mean model age of 1952 ± 39 Ma. In order to confirm the geological significance of this Re—Os age, the effect of metamorphism and later thermal event to the Re—Os system were evaluated. The closure temperature of Re—Os isotopic system for chalcopyrite is still ambiguous, due to the lack of experimental results support. Morelli and Creaser (2007) reported the Re—Os chalcopyrite age, which overlapped the metamorphic age along with a high initial

Table 4
EPMA analysis of siegenite from the Hujiayu copper deposit.

No.	S	Co	Ni	Fe	Cu	Pb	Ag	Zn	As	Se	Total	Formula
Mass percent (wt. %)												
1	41.55	22.79	22.60	9.86	4.11	0.25	<0.04	<0.03	<0.06	<0.03	101.30	$(Co_{1.19}Ni_{1.19}Fe_{0.55}Cu_{0.20})S_4$
2	38.96	19.03	22.12	8.93	4.80	0.43	<0.04	0.15	<0.06	<0.03	94.54	$(Co_{1.06}Ni_{1.24}Fe_{0.53}Cu_{0.25})S_4$
3	39.12	28.63	22.46	3.26	0.05	0.28	<0.04	<0.03	<0.06	0.09	94.06	$(Co_{1.59}Ni_{1.26}Fe_{0.19}Cu_{0.00})S_4$
4	41.72	25.29	23.15	7.51	2.73	0.27	<0.04	<0.03	<0.06	0.05	100.93	$(Co_{1.32}Ni_{1.21}Fe_{0.41}Cu_{0.13})S_4$
5	41.19	27.11	23.90	4.82	0.35	0.27	<0.04	<0.03	<0.06	0.15	97.96	$(Co_{1.43}Ni_{1.27}Fe_{0.27}Cu_{0.13})S_4$
6	41.64	26.91	24.26	5.18	0.71	0.26	<0.04	<0.03	<0.06	0.14	99.28	$(Co_{1.41}Ni_{1.27}Fe_{0.27}Cu_{0.02})S_4$
7	42.15	38.01	18.56	1.57	0.83	0.20	<0.04	<0.03	<0.06	<0.03	101.44	$(Co_{1.96}Ni_{0.96}Fe_{0.09}Cu_{0.04})S_4$
8	41.90	37.02	18.13	1.96	1.23	0.21	<0.04	<0.03	<0.06	<0.03	100.66	$(Co_{1.92}Ni_{0.95}Fe_{0.11}Cu_{0.06})S_4$
9	42.59	40.51	15.23	1.97	0.90	0.27	<0.04	<0.03	<0.06	<0.03	101.65	$(Co_{2.07}Ni_{0.78}Fe_{0.11}Cu_{0.04})S_4$
10	40.60	32.42	22.30	2.78	0	0.217	<0.04	<0.03	<0.06	<0.03	98.36	$(Co_{1.74}Ni_{1.20}Fe_{0.16}Cu_{0.00})S_4$
11	40.40	32.57	22.08	2.75	0	0.243	<0.04	<0.03	<0.06	<0.03	98.19	$(Co_{1.75}Ni_{1.19}Fe_{0.16}Cu_{0.00})S_4$
12	40.64	32.76	22.07	2.52	0	0.047	<0.04	<0.03	<0.06	<0.03	98.06	$(Co_{1.75}Ni_{1.19}Fe_{0.16}Cu_{0.00})S_4$
13	40.35	32.98	21.79	2.67	0.09	0.293	<0.04	<0.03	<0.06	<0.03	98.18	$(Co_{1.78}Ni_{1.18}Fe_{0.15}Cu_{0.00})S_4$
14	40.88	32.63	22.05	2.57	0	0.228	<0.04	<0.03	<0.06	0.06	98.46	$(Co_{1.74}Ni_{1.18}Fe_{0.14}Cu_{0.00})S_4$
15	40.92	33.74	21.25	2.36	0.21	0.314	<0.04	<0.03	<0.06	0.04	98.85	$(Co_{1.79}Ni_{1.13}Fe_{0.13}Cu_{0.01})S_4$

Analysis spots: 1–6 in the rim of the dolomite; 7–15 as mineral inclusions in quartz or chalcopyrite; formula recalculated based on four sulfur atoms.

Table 5
EPMA analysis of sphalerite from the Hujiayu Cu deposit.

No.	As	S	Fe	Pb	Co	Bi	Ni	Cu	Zn	Total	APX. T.
	Mass percent (wt.)										(°C)
1	<0.03	33.65	2.63	0.25	0.10	0.15	<0.04	1.07	61.05	98.91	260
2	<0.03	33.23	2.49	0.25	0.10	0.19	<0.04	0.58	61.85	98.68	258
3	<0.03	33.20	3.39	0.19	0.07	0.13	<0.04	2.16	59.06	98.25	271
4	<0.03	32.76	2.00	0.19	0.10	0.10	<0.04	0.11	60.25	95.54	253
5	0.119	31.05	1.80	0.22	0.09	0.12	<0.04	0.05	57.65	91.12	251
6	<0.03	33.46	1.22	0.20	0.06	0.17	<0.04	0.01	62.56	97.70	242
7	<0.03	32.98	2.04	0.18	0.14	0.06	0.313	0.03	61.02	96.76	253
8	<0.03	33.79	13.40	0.27	0.08	0.14	<0.04	11.72	42.70	102.10	N.S.

APX. T.: the approximate temperature of sphalerite precipitation is estimated with the empirical thermometer proposed by Keith et al. (2014), Fe/Zn = 0.0013 * (T)-0.2953; N. S.: not suitable for determining the temperature; the average value is calculated from No. 1 to No. 7.

radiogenic Os, and inferred that the Re—Os age was reset during greenschist facies metamorphism. On the contrary, Zhu and Sun (2013) concluded that the chalcopyrite Re—Os system was almost unaffected with temperature up to 500 °C in the research of the Lala copper deposit. Considering the closure temperature for pyrrhotite and pyrite (±chalcopyrite) was calculated based on experimental work at around 300–400 °C and 500 °C (Brenan et al., 2000), the Re—Os systems in chalcopyrite can resist the disturbance by relative high temperature thermal events. From field observations (Fig. 3c-d), chalcopyrite-bearing thick veins crosscutting the foliation of host rocks indicated that stage II Cu mineralization occurred post the peak metamorphism. Hence, the peak metamorphism (~540 °C) would not disturb the Re—Os system of chalcopyrite in thick veins. The later volcanic eruption (1800–1750 Ma) did not directly cover the Zhongtiao Group. Thus, the

Table 6
Sulfur isotope data of both veinlet disseminated-veinlet and thick vein type mineralization from the Hujiayu Cu deposit.

Sample no.	Mineral	$\delta^{34}S‰$	Descriptions	Data sources
13HJ15	Pyrite	19.7	Stage I, disseminated-veinlet mineralization	This study
13HJ16	Pyrite	19.4	Stage I, disseminated-veinlet mineralization	This study
13HJ17	Pyrite	15	Stage I, disseminated-veinlet mineralization	This study
13HJ43	Pyrite	10.1	Stage I, disseminated-veinlet mineralization	This study
13HJ54	Pyrite	15.4	Stage I, disseminated-veinlet mineralization	This study
13HJ02	Chalcopyrite	18.7	Stage II, dolomite-quartz-sulfide composit veins	This study
13HJ02	Pyrite	19	Stage II, dolomite-quartz-sulfide composit veins	This study
13HJ03	Chalcopyrite	19.2	Stage II, dolomite-quartz-sulfide composit veins	This study
13HJ03	Pyrite	17.5	Stage II, dolomite-quartz-sulfide composit veins	This study
13HJ05	Pyrite	18.1	Stage II, dolomite-quartz-sulfide composit veins	This study
13HJ09	Chalcopyrite	18.4	Stage II, chalcopyrite-rich quartz veins	This study
13HJ28	Chalcopyrite	15.8	Stage II, chalcopyrite-rich quartz veins	This study
13HJ29	Chalcopyrite	12.9	Stage II, chalcopyrite-rich quartz veins	This study
13HJ30	Chalcopyrite	14.0	Stage II, chalcopyrite-rich quartz veins	This study
13HJ32	Chalcopyrite	13.7	Stage II, chalcopyrite-rich quartz veins	This study
Hu2	Pyrite	15.8	Stage I, disseminated-veinlet mineralization	WGCGZM (1978)
Hu4-1	Pyrite	22.4	Stage I, disseminated-veinlet mineralization	WGCGZM (1978)
Hu11-1	Pyrite	20.7	Stage I, disseminated-veinlet mineralization	WGCGZM (1978)
Hu18	Pyrite	11.3	Stage I, disseminated-veinlet mineralization	WGCGZM (1978)
Hu22	Pyrite	16.4	Stage I, disseminated-veinlet mineralization	WGCGZM (1978)
Hu32	Pyrite	16.11	Stage I, disseminated-veinlet mineralization	WGCGZM (1978)
Hu34	Pyrite	16.3	Stage I, disseminated-veinlet mineralization	WGCGZM (1978)
Hu37	Pyrite	19.2	Stage I, disseminated-veinlet mineralization	WGCGZM (1978)
Hu42	Pyrite	21.5	Stage I, disseminated-veinlet mineralization	WGCGZM (1978)
Hu48	Pyrite	17.6	Stage I, disseminated-veinlet mineralization	WGCGZM (1978)
Hu50	Pyrite	13.9	Stage I, disseminated-veinlet mineralization	WGCGZM (1978)
Hu60	Pyrite	13.6	Stage I, disseminated-veinlet mineralization	WGCGZM (1978)
Hu67	Pyrite	12.1	Stage I, disseminated-veinlet mineralization	WGCGZM (1978)
Hu22	Chalcopyrite	17.1	Stage I, disseminated-veinlet mineralization	WGCGZM (1978)
Hu25	Chalcopyrite	13.7	Stage I, disseminated-veinlet mineralization	WGCGZM (1978)
Hu32	Chalcopyrite	16.3	Stage I, disseminated-veinlet mineralization	WGCGZM (1978)
4157-Cp	Chalcopyrite	20.9	Stage I, disseminated-veinlet mineralization	WGCGZM (1978)
4158-Cp	Chalcopyrite	22.2	Stage I, disseminated-veinlet mineralization	WGCGZM (1978)
3233-Cp	Chalcopyrite	12.8	Stage I, disseminated-veinlet mineralization	WGCGZM (1978)
3409-Cp	Chalcopyrite	17.7	Stage I, disseminated-veinlet mineralization	WGCGZM (1978)
3857-Cp	Chalcopyrite	18.7	Stage I, disseminated-veinlet mineralization	WGCGZM (1978)
3640-Cp	Chalcopyrite	19.9	Stage I, disseminated-veinlet mineralization	WGCGZM (1978)
Hu8	Pyrite	11.3	Stage II, vein type mineralization	WGCGZM (1978)
Hu38	Pyrite	8.1	Stage II, vein type mineralization	WGCGZM (1978)
Hu59-1	Pyrite	7.3	Stage II, vein type mineralization	WGCGZM (1978)
Hu68	Pyrite	4.9	Stage II, vein type mineralization	WGCGZM (1978)
Hu73	Pyrite	8.4	Stage II, vein type mineralization	WGCGZM (1978)
3176-Py	Pyrite	12	Stage II, vein type mineralization	WGCGZM (1978)
3213-Py	Pyrite	11.8	Stage II, vein type mineralization	WGCGZM (1978)
3215-Py	Pyrite	9.7	Stage II, vein type mineralization	WGCGZM (1978)
3242-Py	Pyrite	11.8	Stage II, vein type mineralization	WGCGZM (1978)
3212-Py	Pyrite	3.4	Stage II, vein type mineralization	WGCGZM (1978)

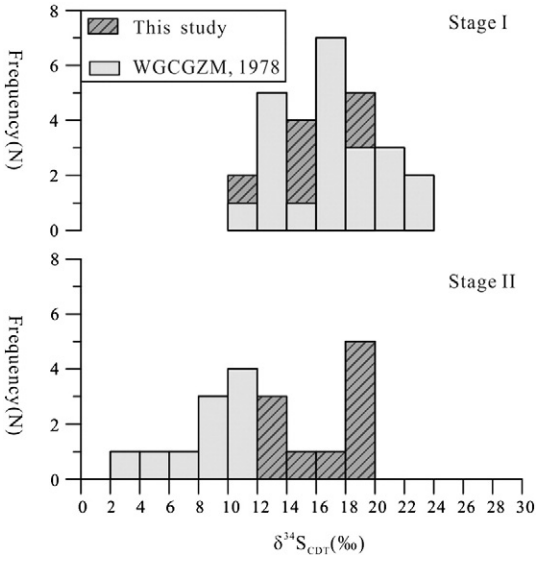

Fig. 7. Histogram of sulfur isotope compositions of sulfide minerals from two distinct mineralizations in the Hujiayu Cu deposit.

far-field thermal event would have less effect on this isotopic system. From the previous review of the geological settings, the Zhongtiao Mountains district has undergone the long-lived metamorphism and deformation from 1970 Ma to 1850 Ma (Sun et al., 1992; Liu et al., 2007). The age of thick vein type copper mineralization is considered coeval with regional metamorphism. If the primary mineralization occurred during the syn-sedimentary stage as suggested by previous studies, the Re—Os chalcopyrite age would be reset during the peak metamorphism (~540 °C). However, if the Re—Os age was reset, the initial radiogenic Os would be high inferred from the chalcopyrite Re—Os geochronology study of an example from metamorphosed VMS ores in Trans Hudson orogen, Canada (Morelli and Creaser, 2007). Actually, the initial ^{187}Os of the Re—Os chalcopyrite age for stage II Cu mineralization is relatively low and constrained at 0.001 ± 0.01 from the ^{187}Re versus ^{187}Os plot (Fig. 8b). To sum up, this chalcopyrite Re—Os age can directly represent the timing of vein type copper mineralization at Hujiayu.

6.3. Sources of sulfur and metals

Sulfur isotope systematics can be used to trace the source of sulfur. In accordance with previous results in Table 6, sulfides from the stage I of disseminated-veinlets mineralization have δ^{34}S value ranging from 10.1 to 22.2‰. The δ^{34}S value distribution is clustered around 10 to 22‰, with an average of 16.9 ± 3.4‰ (1σ, n = 27). The high δ^{34}S values suggest that the ^{34}S-enriched source was responsible for the sulfur inventory. Sulfides of this stage cannot have the same sulfur source as diagenetic pyrite in carbonaceous shale commonly having negative δ^{34}S value (McGowan et al., 2003). Alternately, high δ^{34}S values of sulfides can be derived from the thermochemical reduction of a sulfate-enriched fluid in a closed system (McGowan et al., 2003). Sulfate reduction by thermochemical processes invariably produces some spread in δ^{34}S (Hoefs, 2008; Johnson et al., 2012). However, the ^{34}S values are uniform enough (with a standard deviation of 3.4‰) to suggest a metamorphic homogenization hypothesis. Metamorphic reequilibration of sulfides at high grade resulted in homogenization of heavy ^{34}S, since the host rock was metamorphosed at relative high temperature of ~540 °C (Dechow and Jensen, 1965; Johnson et al., 2012). The isotopic data of the early stage sulfides support the models that sulfides precipitated through thermochemical reduction of sulfate at the sedimentary stage followed by metamorphic homogenization of δ^{34}S isotopic signatures.

Sulfides from the stage II of thick vein mineralization have δ^{34}S values in highly variable ranging from 3.4 to 19.2‰. The discordance of the new sulfur isotopic data and previous results suggests that the sulfur source of thick vein mineralization is complicated. Two plausible explanations for the widely spread sulfur isotope data of stage II are proposed here. If the sulfur was from a multisource, lower δ^{34}S values could be attributed to an influx of lighter sulfur from the metamorphic fluid or deep seated sulfur source and the heavy ^{34}S was derived from ^{34}S-enriched sedimentary source, e.g. the marine evaporites. If the sulfur source remains the same with stage I, the relatively increasing of oxygen fugacity in stage II will also cause a drop down of δ^{34}S values of sulfides (Ohmoto, 1986; Hodkiewicz et al., 2009).

Lacking effective isotopic tracers for the metal, sources of the thick vein mineralization in the Hujiayu Cu deposit are difficult to be solved. The copper-bearing fluid is rich in Co, Ni and Se as the existence of siegenite and clausthalite. In the study area, the copper bodies are mostly hosted in the graphite schist, sandwiched in the dolomitic marble. The graphite schist, which originally was a carbonaceous shale deposited in a restricted, marine, anoxic basin, should be responsible for the copper and other trace metal element source. The carbonaceous shale commonly is enriched in Se, and hence, served as a preferable source for the Se (Simon et al., 1997; Cabral et al., 2012). Furthermore, carbonaceous shales capable of trapping Cu and Co have been well documented in sedimentary stratiform Cu—Co (SSC) deposits in the Central African Copper belt (e.g. Kirkham, 1989; Cailteux et al., 2005) or in the Permian Zechstein basin of Europe (Kupferschiefer: Sawlowice, 2013), and in the Black Butte shale-hosted copper deposit, Montana, USA (White et al., 2014). Jiang et al. (2014) firstly proposed that the ore-forming process similar to SSC deposits may occur in the early stage mineralization within the "Hu-Bi type" Cu deposits, evidence from the deposit geology, fluid inclusions study at the Hujiayu Cu deposits. Thus, it is speculated that Cu—Co was originally enriched in carbonaceous shale, then completely remobilized during subsequent metamorphism and deformation and precipitated in the metamorphic hydrothermal veins.

6.4. Genetic models

Distinct genetic models have been proposed for the "Hu-Bi type" strata-bound copper deposits in the Zhongtiao Mountains. The main conflict between different models is the interpretation of the Cu deposit varying from a metamorphosed origin (Sun et al., 1989; Zhao and Zhen, 2006; Jiang et al., 2014) to a metamorphogenic origin (Hu and Sun, 1987; Sun et al., 1990).

Table 7
Re—Os isotopic data of chalcopyrite from the dolomite-quartz-sulfide veins, the Hujiayu Cu deposit.

Sample no.	Mineral	Re ± 1σ (ppb)	Common Os ± 1σ (ppb)	^{187}Re/^{188}Os ± 1σ	^{187}Os/^{188}Os ± 1σ	^{187}Re ± 1σ (ppb)	^{187}Os ± 1σ (ppb)	Single mineral model age (Ma)
13HJ28	Chalcopyrite	14.43 ± 0.21	0.0046 ± 0.0001	14624 ± 471	498 ± 16	9.04 ± 0.13	0.321 ± 0.004	2101 ± 26
13HJ29	Chalcopyrite	8.25 ± 0.11	0.0034 ± 0.0002	11453 ± 601	376 ± 19	5.17 ± 0.07	0.168 ± 0.002	1928 ± 18
13HJ30	Chalcopyrite	5.26 ± 0.12	0.0038 ± 0.0002	6531 ± 451	212 ± 11	3.29 ± 0.07	0.108 ± 0.001	1949 ± 16
13HJ31	Chalcopyrite	13.44 ± 0.09	0.0033 ± 0.0003	19204 ± 1970	641 ± 55	8.42 ± 0.06	0.277 ± 0.006	1951 ± 41
13HJ32	Chalcopyrite	7.97 ± 0.06	0.0042 ± 0.0002	8949 ± 421	273 ± 12	4.99 ± 0.03	0.154 ± 0.002	1835 ± 29
13HJ33	Chalcopyrite	7.45 ± 0.10	0.0037 ± 0.0002	9459 ± 406	312 ± 13	4.66 ± 0.06	0.156 ± 0.002	1985 ± 20

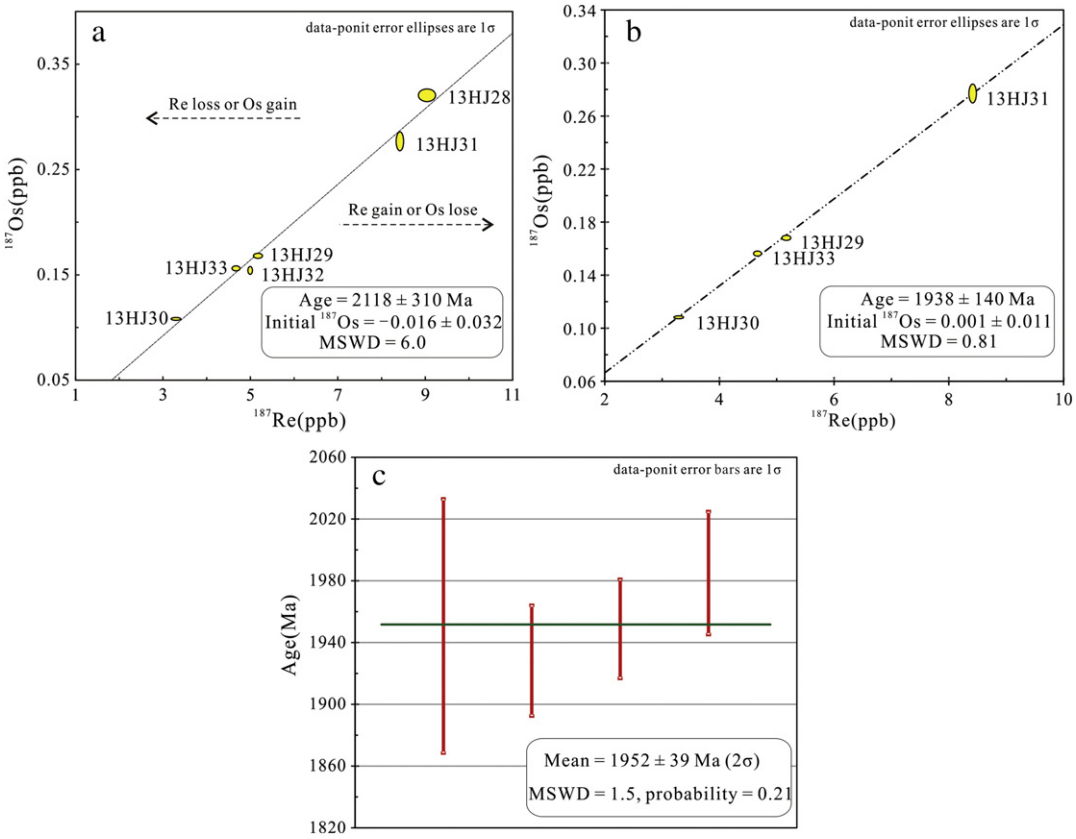

Fig. 8. ^{187}Re—^{187}Os isochron plots (a–b) and a diagram of weighted mean model age (c) for chalcopyrite separates from the Hujiayu Cu deposit. A ^{187}Re—^{187}Os isochron diagram of total chalcopyrite samples shows excess scatter in the data as a result of open-system behavior of the Re—Os isotopic system (a). Four selected chalcopyrite samples define a ^{187}Re—^{187}Os isochron age with an age of 1938 ± 140 Ma (1 σ) and an MSWD of 0.81 (b). A diagram of weighted mean model ages gives an age of 1952 ± 39 Ma (1 σ) with a MSWD of 1.5 (c).

Regarding genesis of the thick vein type mineralization (stage II) of Hujiayu Cu deposit, several lines of evidence support that is of metamorphogenic origin: (1) it is structurally controlled, crosscutting the foliations of host rock; (2) the ore-forming fluid of the quartz-sulfide veins (stage IIb) is characterized by the $CO_2(CH_4)$—H_2O—NaCl system, likely deriving from metamorphic fluids (Qiu et al., 2015); (3) Re—Os dating of chalcopyrite selected from dolomite-quartz vein reveals that copper mineralization occurred synchronously with the regional metamorphism.

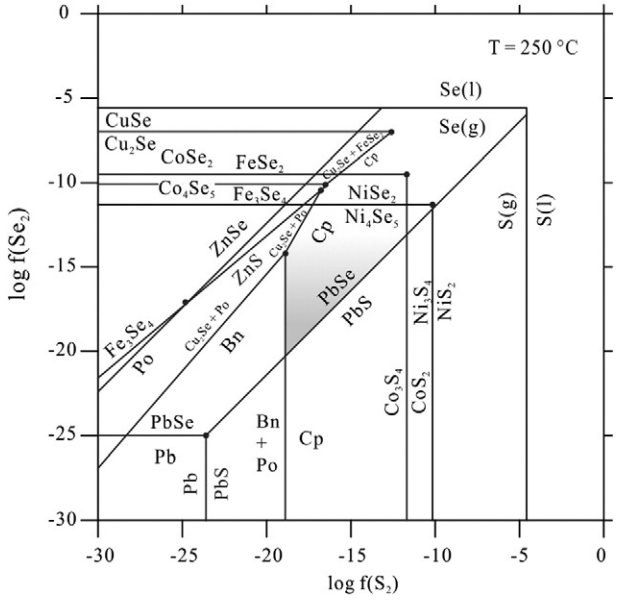

Fig. 9. LogfS_2(g)–logfSe_2(g) diagram showing the relative stability of selenides and sulfides at 250 °C. The shaded area represents the fugacity range of the stage II mineralization in the Hujiayu Cu deposit. All thermodynamic data to construct the diagram were taken from Simon and Essene (1996), Nekrasov (1996) and Xu et al. (2014). Abbreviations: Bn = bornite, Cp = chalcopyrite, Po = pyrrhotite.

However, the genesis of the early stage mineralization with disseminated to veinlet sulfides in graphite schist (stage I) is still debated. The mineralogy in the early stage is simple and consists of major pyrite and minor chalcopyrite, lacking the classic native copper–chalcocite–bornite–chalcopyrite mineral zoning that is commonly displayed in the SSC deposits (e.g. Cailteux et al., 2005; Hitzman et al., 2010; White et al., 2014). In fact, the early stage of sulfide minerals is distributed in the quartz–albite–dolomite metamorphic veinlets, regarded as synmetamorphic stage in this study. Graphite geothermometry shows that the graphite schist had undergone ~540 °C thermal event. At such high temperature, the original sulfide mineral in the graphite schist (originally carbonaceous shale) would be breakdown and liberate sulfur into metamorphic fluid (e.g. Tomkins, 2010). Therefore, the mineralization style of the early stage in the "Hu-Bi type" copper deposits more likely is the results of metamorphic processes and is difficult to preserve the SSC mineralization.

The Zhongtiao Mountains within the Paleoproterozoic Jinyu mobile belt have experienced the long-lived metamorphism from 1970 Ma to 1850 Ma (Sun et al., 1992; Liu et al., 2007). However, the cause of metamorphism is under debating. The multi-phase collision model suggested that the metamorphic age of ~1.95 Ga was interpreted to represent the time for an older metamorphic event related to arc-arc or arc-continent collision and the metamorphic age of ~1.85 Ga represented the final amalgamation event of the North China craton (Zhao et al., 2005; Qian et al., 2013). Another model favored a long-lived

orogenic process which lasts a period over 100 Ma. The metamorphic age of ~1.95 Ga represent the main collision or crustal thickening and the younger age of ~1.85 Ga could be an indicator of cooling of the high-grade terranes (Zhai, 2011; Qian et al., 2013). Despite the differences between two models, they reached a consensus that the ~1.95 Ga regional metamorphism in the study area is a type of orogenic metamorphism related to the orogenic event or the closure of the rift. Thus, ~1.95 Ga copper mineralization in the Hujiayu deposit occurred during the orogenic metamorphism.

Based on the discussions above, we proposed that the Hujiayu Cu deposit is a metamorphogenic deposit and the ore-forming process is accompanying with the metamorphic evolution of the Paleoproterozoic mobile belt (Fig. 10). The primary copper and cobalt was probably pre-enrichment in carbonaceous rock at diagenetic stage or the SSC mineralization occurred in the carbonaceous rock. Subsequently, the copper and cobalt were remobilized during the orogenic prograde metamorphism. At metamorphic peak, the carbonaceous in the host rocks transformed into graphite and sulfides precipitated in metamorphic veinlets. The major hydrothermal copper mineralization occurred at the fractures within host rock during the retrograde cooling.

7. Conclusion

The Hujiayu Cu deposit, consisting of disseminated-veinlets and thick vein type mineralization within graphite schist and dolomitic marble, is a Paleoproterozoic metamorphogenic Cu deposit, in the Zhongtiao Mountains, China. The disseminated mineralization occurred closely to the peak metamorphism and the thick vein mineralization formed at the age of 1952 ± 39 Ma during the retrograde metamorphism. At least three generations of pyrite were identified, corresponding to the synmetamorphic stage, hydrothermal dolomitic alteration and siliceous-copper stage. At the hydrothermal conditions, cobalt prefers to incorporate into the pyrite structure at high temperature, whereas forming independent minerals, such as siegenite, at the relatively low temperature. During the ore-forming process, the sulfur fugacity is high at the syn-metamorphic stage, and then the selenium fugacity is strong increasing with a marked drop of sulfur fugacity after the major copper mineralization. The sulfides in the syn-metamorphic stage may experience metamorphic reequilibration at high grade metamorphism resulted in homogenization of heavy ^{34}S, while the sulfur in the hydrothermal stage is complicated and probably reflects multiple sources, presuming a mixed metamorphic fluid, ^{34}S-enriched sedimentary source and deep seated sulfur source. The source of Cu and Co is still unresolved. It is speculated that Cu—Co was originally enriched in carbonaceous shale, then completely remobilized during subsequent prograde metamorphism and precipitated in the metamorphic hydrothermal veins at retrograde cooling.

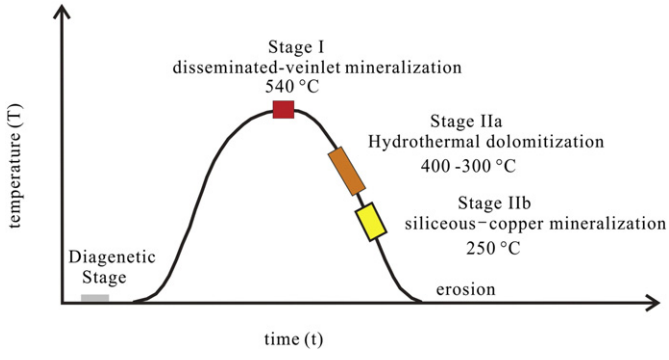

Fig. 10. Metamorphic history of carbonaceous shale host rock in the Hujiayu Cu deposit on a temperature-time path. The evolution of ore-forming processes are accompanying the metamorphic cycle of the host rocks. The pre-enrichment of Cu and Co in carbonaceous shale is at the onset of regional metamorphism. During prograde metamorphism by devolatilization reactions, sources rock involves liberation of essentially H_2O, CO_2 and potentially Cu and Co metallic elements. The major hydrothermal copper mineralization occurs during the retrograde cooling.

Acknowledgments

We are indebted to Prof. Liang Qi and Dr. Ting-Guang Lan for their kindly helps with chalcopyrite Re—Os dating. Dr. Qian Mao and Mr. Yuguang Ma are acknowledged for their generous helps during EPMA analyses. We thank Shuanglong Guo, Fengchun Zhao and Yongping Chen from the Zhongtiaoshan Non-ferrous Metals Group Co., Ltd for their helps during field investigation. Edit-in-Chief Prof. Franco Pirajno and two anonymous referees are thanked for their constructive and valuable comments which greatly contributed to the improvements of the manuscript. This research was financed by Major State Basic Research Development Program (2012CB416605) and Natural Science Foundation of China (41402083).

References

Aoya, M., Kouketsu, Y., Endo, S., Shimizu, H., Mizukami, T., Nakamura, D., Wallis, S., 2010. Extending the applicability of the Raman carbonaceous-material geothermometer using data from contact metamorphic rocks. J. Metamorph. Geol. 28 (9), 895–914.
Asadi, S., Moore, F., Fattahi, N., 2013. Fluid inclusion and stable isotope constraints on the genesis of the Jian copper deposit, Sanandaj–Sirjan metamorphic zone, Iran. Geofluids 13, 66–81.
Bajwah, Z.U., Seccombe, P.K., Offler, R., 1987. Trace element distribution, Co: Ni ratios and genesis of the Big Cadia iron–copper deposit, New South Wales, Australia. Mineral. Deposita 22 (4), 292–300.
Bartholomé, P., Katekesha, F., Ruiz, J.L., 1971. Cobalt zoning in microscopic pyrite from Kamoto, Republic of the Congo (Kinshasa). Mineral. Deposita 6 (3), 167–176.
Barton Jr., P.B., Bethke, P.M., 1987. Chalcopyrite disease in sphalerite: pathology and epidemiology. Am. Mineral. 72 (5-6), 451–467.
Beyssac, O., Goffé, B., Chopin, C., Rouzaud, J.N., 2002. Raman spectra of carbonaceous material in metasediments: a new geothermometer. J. Metamorph. Geol. 20 (9), 859–871.
Bortnikov, N.S., Genkin, A.D., Dobrovol'Skaya, M.G., Muravitskaya, G.N., Filimonova, A.A., 1991. The nature of chalcopyrite inclusions in sphalerite; exsolution, coprecipitation, or "disease"? Econ. Geol. 86 (5), 1070–1082.
Brenan, J.M., Cherniak, D.J., Rose, L.A., 2000. Diffusion of osmium in pyrrhotite and pyrite: implications for closure of the Re–Os isotopic system. Earth Planet. Sci. Lett. 180 (3), 399–413.
Brown, A.C., Bartholomé, P., 1972. Inhomogeneities in cobaltiferous pyrite from the Chibuluma Cu—Co deposit, Zambia. Mineral. Deposita 7 (1), 100–105.
Craig, J.R., Vaughan, D.J., Higgins, J.B., 1979. Phase relations in the Cu—Co—S system and mineral associations of the carrollite ($CuCo_2S_4$)–linnaeite (Co_3S_4) series. Econ. Geol. 74 (3), 657–671.
Cabral, A.R., Koglin, N., Brätz, H., 2012. Iridium enrichment and poor fractionation from gold, platinum and palladium in clausthalite (PbSe), Tilkerode, eastern Harz, Germany. Mineral. Petrol. 105 (3-4), 113–119.
Cailteux, J.L.H., Kampunzu, A.B., Lerouge, C., Kaputo, A.K., Milesi, J.P., 2005. Genesis of sediment-hosted stratiform copper–cobalt deposits, central African Copperbelt. J. Afr. Earth Sci. 42 (1), 134–158.
Cartwright, I., Oliver, N., 2000. Metamorphic fluids and their relationship to the formation of metamorphosed and metamorphogenic ore deposits. In: Spry, P.G., Marshall, B., Vokes, F.M. (Eds.), Metamorphosed and Metamorphogenic Ore Deposits. Rev. Econ. Geol. 11, pp. 81–95.
Clark, C., Grguric, B., Mumm, A.S., 2004. Genetic implications of pyrite chemistry from the Palaeoproterozoic Olary Domain and overlying Neoproterozoic Adelaidean sequences, northeastern South Australia. Ore Geol. Rev. 25 (3), 237–257.
Craig, J.R., Vokes, F.M., Solberg, T.N., 1998. Pyrite: physical and chemical textures. Mineral. Deposita 34 (1), 82–101.
Dechow, E., Jensen, M.L., 1965. Sulfur isotopes of some central African sulfide deposits. Econ. Geol. 60 (5), 894–941.
Ding, C., Nie, F., Bagas, L., Dai, P., Jiang, S., Ding, C., Liu, C., Peng, Y., Zhang, G., Shao, G., 2016. Pyrite Re–Os and zircon U–Pb dating of the Tugurige gold deposit in the western part of the Xing'an–Mongolia Orogenic Belt, China and its geological significance. Ore Geol. Rev. 72, 669–681.
Du, A. D., Wu, S. Q., Sun, D. Z., Wang, S. X., Qu, W. J., Markey, R., Stein, H., Morgan, J., Malinovskiy, D., 2004. Preparation and certification of Re—Os dating reference materials: molybdenites HLP and JDC. Geostand. Geoanal. Res. 28, 41—52.
Fanlo, I., Subías, I., Gervilla, F., Paniagua, A., García, B., 2004. The composition of Co–Ni–Fe sulfarsenides, diarsenides and triarsenides from the San Juan de Plan deposit, Central Pyrenees, Spain. Can. Mineral. 42(4), 1221—1240.
Förster, H.J., 2005. Mineralogy of the U–Se-polymetallic deposit Niederschlema–Alberoda, Erzgebirge, Germany. IV. The continuous clausthalite–galena solid-solution series. Neues Jahrbuch für Mineralogie-Abhandlungen. J. Mineral. Geochem. 181 (2), 125–134.
Goldfarb, R.J., Baker, T., Dube, B., Groves, D.I., Hart, C.J., Gosselin, P., 2005. Distribution, character and genesis of gold deposits in metamorphic terranes. Econ. Geol. 100th anniversary vol. 407-450.

Gregory, M.J., Schaefer, B.F., Keays, R.R., Wilde, A.R., 2008. Rhenium–osmium systematics of the Mount Isa copper orebody and the Eastern Creek Volcanics, Queensland, Australia: implications for ore genesis. Mineral. Deposita 43 (5), 553–573.
Groves, D.I., Goldfarb, R.J., Robert, F., Hart, C.J., 2003. Gold deposits in metamorphic belts: overview of current understanding, outstanding problems, future research, and exploration significance. Econ. Geol. 98, 1–29.
Heinrich, C.A., Andrew, A.S., Wilkins, R.W., Patterson, D.J., 1989. A fluid inclusion and stable isotope study of synmetamorphic copper ore formation at Mount Isa, Australia. Econ. Geol. 84, 529–550.
Hem, S.R., Makovicky, E., 2004. The system Fe–Co–Ni–As–SI Phase relations in the (Fe, Co, Ni) As0. 5S1. 5 section at 650 and 500 C. Can. Mineral. 42 (1), 43–62.
Hitzman, M.W., Selley, D., Bull, S., 2010. Formation of sedimentary rock-hosted stratiform copper deposits through Earth history. Econ. Geol. 105 (3), 627–639.
Hodkiewicz, P.F., Groves, D.I., Davidson, G.J., Weinberg, R.F., Hagemann, S.G., 2009. Influence of structural setting on sulphur isotopes in Archean orogenic gold deposits, Eastern Goldfields Province, Yilgarn, Western Australia. Mineral. Deposita 44 (2), 129–150.
Hoefs, J., 2008. Stable Isotope Geochemistry. sixth ed. Springer Science & Business Media, Berlin, pp. 1–285.
Hu, W.X., Sun, D.Z., 1987. Mineralization and evolution of the Early Proterozoic copper deposits in the Zhongtiao Mountains. Acta Geol. Sin. Engl. Ed. 61, 61–76.
Huang, X.W., Gao, J.F., Qi, L., Zhou, M.F., 2015. In-situ LA-ICP-MS trace elemental analyses of magnetite and Re—Os dating of pyrite: the Tianhu hydrothermally remobilized sedimentary Fe deposit, NW China. Ore Geol. Rev. 65, 900–916.
Jiang, Y., Niu, H., Bao, Z., Li, N., Shan, Q., Yang, W., Yan, S., 2014. Fluid evolution of the Paleoproterozoic Hujiayu copper deposit in the Zhongtiaoshan region: Evidence from fluid inclusions and carbon–oxygen isotopes. Precambrian Res. 255, 734–747.
Johnson, C.A., Bookstrom, A.A., Slack, J.F., 2012. Sulfur, carbon, hydrogen, and oxygen isotope geochemistry of the Idaho cobalt belt. Econ. Geol. 107 (6), 1207–1221.
Keith, M., Haase, K.M., Schwarz-Schampera, U., Klemd, R., Petersen, S., Bach, W., 2014. Effects of temperature, sulfur, and oxygen fugacity on the composition of sphalerite from submarine hydrothermal vents. Geology 42 (8), 699–702.
Kirkham, R.V., 1989. Distribution, settings, and genesis of sediment-hosted stratiform copper deposits. Geol. Assoc. Can. Spec. Pap. 36, 3–38.
Klemm, D.D., 1965. Synthesen und Analysen in den Dreiecksdiagrammen FeAsS–CoAsS–NiAsS und FeS_2–CoS_2–NiS_2. Neues Jb. Mineral. Abh. 103, 205–255.
Lambert, D.D., Foster, J.G., Frick, L.R., Hoatson, D.M., Purvis, A.C., 1998. Application of the Re—Os isotopic system to the study of Precambrian magmatic sulfide deposits of Western Australia. Aust. J. Earth Sci. 45, 265–284.
Li, Q., Chen, X., Liu, S., Wang, Z., Zhou, Y., Zhang, J., Wang, T., 2009. Evaluating the provenance of metasedimentary rocks of the Jiangxian Group from the Zhongtiao Mountain using whole-rock geochemistry and detrital zircon Hf isotope. Acta Geol. Sin. Engl. Ed. 83 (3), 550–561.
Liu, C., Zhao, G., Sun, M., Zhang, J., Yin, C., 2012. U—Pb geochronology and Hf isotope geochemistry of detrital zircons from the Zhongtiao Complex: constraints on the tectonic evolution of the Trans-North China Orogen. Precambrian Res. 222, 159–172.
Liu, S., Zhang, C., Liu, C., Li, Q., Lv, Y., Yu, S., Tian, W., Feng, Y., 2007. EPMA Th—U—Pb monazite dating of Zhongtiao and Lüliang Precambrian Metamorphic Complexes. Earth Sci. Front. 14 (1), 64–74 (in Chinese with English abstract).
Liu, X., Fan, H.R., Qiu, Z.J., Yang, Y.F., Hu, F.F., Guo, S.L., Zhao, F.C., 2015. Formation ages of the Jiangxian and Zhongtiao groups in the Zhongtiao Mountain region, North China Craton: insights from SIMS U—Pb dating on zircons of intercalated plagioclase amphibolites. Acta Petrol. Sin. 31 (6), 1564–1572 (in Chinese with English abstract).
Liu, X., Fan, H.R., Santosh, M., Yang, K.F., Qiu, Z.J., Hu, F.F., Wen, B.J., 2016. Geological and geochronological constraints on the genesis of the giant Tongkuangyu Cu deposit (Palaeoproterozoic), North China Craton. Int. Geol. Rev. 58 (2), 155–170.
Ludwig, K.R., 2003. Isoplot/Ex Version 3.23. A Geochronological Toolkit for Microsoft Excel. Berkeley Geochronology Center (Special Publication).
Marshall, B., Vokes, F.M., Larocque, A.C.L., 2000. Regional metamorphic remobilisation: upgrading and formation of ore deposits. In: Spry, P.G., Marshall, B., Vokes, F.M. (Eds.), Metamorphosed and Metamorphogenic Ore Deposits. Rev. Econ. Geol. 11, pp. 19–38.
McGowan, R.R., Roberts, S., Foster, R.P., Boyce, A.J., Coller, D., 2003. Origin of the copper–cobalt deposits of the Zambian Copperbelt: an epigenetic view from Nchanga. Geology 31 (6), 497–500.
Mei, H.L., 1994. Metamorphic P–T–t paths and tectonic evolution of early Proterozoic rocks from the Zhongtiao Mountains, Southern Shanxi. Geol. Rev. 40 (1), 36–47 (in Chinese with English abstract).
Morelli, R.M., Creaser, R.A., 2007. Testing the robustness of Re–Os low level sulfide chronometers: an example from metamorphosed VMS ores, Trans Hudson orogen, Canada [abs.]. Geol. Soc. Am. Program Abstr. 39, 276.
Morelli, R.M., Creaser, R.A., Selby, D., Kelley, K.D., Leach, D.L., King, A.R., 2004. Re—Os sulfide geochronology of the Red Dog sediment-hosted Zn—Pb—Ag deposit, Brooks Range, Alaska. Econ. Geol. 99, 1569–1576.
Nekrasov, I.Y., 1996. Geochemistry, Mineralogy and Genesis of Gold Deposits. CRC Press, pp. 217–256.
Nold, J.L., 1990. The Idaho cobalt belt, northwestern United States—a metamorphosed Proterozoic exhalative ore district. Mineral. Deposita *25* (3), 163–168.
Ohmoto, H., 1986. Stable isotope geochemistry of ore deposits. In: Valley, J.W., Taylor, H.P.J., O'Neil, J.R. (Eds.), Stable Isotopes in High Temperature Geological Processes. Rev. Mineral., pp. 491–559.
Pirajno, F., 2000. Ore Deposits and Mantle Plumes. Springer Science & Business Media, pp. 291–317.
Pohl, W., 1992. Defining metamorphogenic mineral deposits—an introduction. Mineral. Petrol. 45, 145–152.
Qi, L., Zhou, M.F., Gao, J., Zhao, Z., 2010. An improved Carius tube technique for determination of low concentrations of Re and Os in pyrites. J. Anal. At. Spectrom. 25, 585–589.
Qian, J., Wei, C., Zhou, X., Zhang, Y., 2013. Metamorphic P–T paths and new Zircon U—Pb age data for garnet–mica schist from the Wutai Group, North China Craton. Precambrian Res. 233, 282–296.
Qiu, Z.J., Fan, H.R., Liu, X., Wen, B.J., Hu, F.F., Yang, Y.F., Guo, S.L., Zhao, F.C., 2015. Fluid inclusion and carbon–oxygen isotope studies of the Hujiayu Cu Deposit, Zhongtiao Mountains, China: implications for syn-metamorphic copper remobilization. Acta Geol. Sin. Engl. Ed. 89 (3), 726–745.
Raymond, O.L., 1996. Pyrite composition and ore genesis in the Prince Lyell copper deposit, Mt Lyell mineral field, western Tasmania, Australia. Ore Geol. Rev. 10 (3), 231–250.
Ridley, J.R., Diamond, L.W., 2000. Fluid chemistry of orogenic lode gold deposits and implications for genetic models. Gold in. vol. 2000, pp. 141–162.
Roberts, F.I., 1982. Trace element chemistry of pyrite: a useful guide to the occurrence of sulfide base metal mineralization. J. Geol. Chem. Explor. 17, 49–62.
Sawlowice, Z., 2013. REE and their relevance to the development of the Kupferschiefer copper deposit in Poland. Ore Geol. Rev. 55, 176–186.
Schoenberg, R., Nägler, T.F., Kramers, J.D., 2000. Precise Os isotope ratio and Re—Os isotope dilution measurements down to the picogram level using multicollector inductively coupled plasma mass spectrometry. Int. J. Mass Spectrom. 197, 85–94.
Shi, Z., Li, L., 2000. Mineralogical characters of cobalt pyrite in Hubi copper deposit of Zhongtiaoshan and importance of prospecting. Nonferrous Min. 29 (5), 1–5 (in Chinese with English abstract).
Simon, G., Essene, E.J., 1996. Phase relations among selenides, sulfides, tellurides, and oxides; I, Thermodynamic properties and calculated equilibria. Econ. Geol. 91 (7), 1183–1208.
Simon, G., Kesler, S.E., Essene, E.J., 1997. Phase relations among selenides, tellurides, and oxides; II, Applications to selenide-bearing ore deposits. Econ. Geol. *92* (4), 468–484.
Slack, J.F., 2012. Strata-bound Fe—Co—Cu—Au—Bi-Y-REE deposits of the Idaho cobalt belt: Multistage hydrothermal mineralization in a magmatic-related iron oxide copper–gold system. Econ. Geol. 107 (6), 1089–1113.
Smoliar, M.I., Walker, R.J., Morgan, J.W., 1996. Re\Os ages of group IIA, IIIA, IVA, and IVB iron meteorites. Science 271, 1099–1102.
Stein, H.J., Morgan, J.W., Scherstén, A., 2000. Re—Os dating of low-level highly radiogenic (LLHR) sulfides: the Harnäs gold deposit, southwest Sweden, records continental-scale tectonic events. Econ. Geol. 95 (8), 1657–1671.
Sun, D.Z., Hu, W.X., Tang, M., Zhao, F.Q., Condie, K.C., 1990. Origin of Late Archean and Early Proterozoic rocks and associated mineral deposits from the Zhongtiao Mountains, east-central China. Precambrian Res. 47 (3), 287–306.
Sun, D.Z., Li, H.M., Lin, Y.X., Zhou, H.F., Zhao, F.Q., Tang, M., 1992. Precambrian geochronology, chronotectonic framework and model of chronocrustal structure of the Zhongtiao Mountains. Acta Geol. Sin. Engl. Ed. 5 (1), 23–37.
Sun, H., Ge, C., Ji, S., 1989. Characteristics and genesis of breccias from the Hujiayu–Bizigou type stratabound copper deposits in Zhongtiao area. Mineral Deposits 8, 19–28 (in Chinese with English abstract).
Tao, Q., 1985. Geological Ages of Precambrian Strata in the Zhongtiao Mountains. Tianjin Institute of Geology and Mineral Resources, C.A.G.S., Geological Publishing House (in Chines).
Tomkins, A.G., 2010. Windows of metamorphic sulfur liberation in the crust: implications for gold deposit genesis. Geochim. Cosmochim. Acta 74 (11), 3246–3259.
Tian, W., Liu, S.W., Zhang, H.F., 2006. Paleoproterozoic potassic granitoids in the Sushui complex from the Zhongtiao Mountains, Northern China: geochronology, geochemistry and petrogenesis. Acta Geol. Sin. Engl. Ed. 80 (6), 875–885.
Wen, N., Boyce, A.J., Fallick, A.E., Ashworth, J.R., Ixer, R.A., 1996. The genesis of Cu-bearing quartz veins by metamorphic remobilization from stratiform red bed deposits, SW County Cork, Ireland. Mineral. Petrol. 57 (1-2), 73–89.
White, J., Gammons, C.H., Zieg, G.A., 2014. Paragenesis of cobalt and nickel in the Black Butte shale-hosted copper deposit, Belt Basin, Montana, USA. Mineral. Deposita 49 (3), 335–351.
Working Group on Copper Geology of the Zhongtiao Mountains, 1978,. Copper Geology of the Zhongtiao Mountains. Geological Publishing House, Beijing, pp. 89–135 (in Chinese).
Xu, W.G., Fan, H.R., Hu, F.F., Santosh, M., Yang, K.F., Lan, T.G., Wen, B.J., 2014. Gold mineralization in the Guilaizhuang deposit, southwestern Shandong Province, China: insights from phase relations among sulfides, tellurides, selenides and oxides. Ore Geol. Rev. 56, 276–291.
Yu, S.Q., Liu, S.W., Tian, W., Li, Q.G., Feng, Y.G., 2006. SHRIMP zircon U—Pb chronology and geochemistry of the Henglingshan and Beiyu granitoids in the Zhongtiao Mountains, Shanxi Province. Acta Geol. Sin. Engl. Ed. 80 (6), 912–924.
Zhai, M.G., 2011. Cratonization and the ancient North China Continent: a summary and review. Sci. China Earth Sci. 54 (8), 1110–1120.
Zhai, M.G., Peng, P., 2007. Paleoproterozoic events in the North China craton. Acta Petrol. Sin. 23 (11), 2665–2682.
Zhai, M.G., Santosh, M., 2013. Metallogeny of the North China Craton: link with secular changes in the evolving Earth. Gondwana Res. 24 (1), 275–297.
Zhang, H., 2012. Metallogenesis of paleoproterozoic copper deposits in the northern Zhongtiaoshan Mountains, Shanxi Province (PhD thesis) JiLin Univ., pp. 72–139 (in Chinese with English abstract).
Zhang, L., Li, B.L., Zhang, H., Hu, A.X., 2013a. Re-Os isotopic dating and its geological significance of molybdenite, from Tongmugou copper deposit in Zhongtiaoshan, Shanxi. Glob. Geol. 32 (4), 740–746 (in Chinese with English abstract).
Zhang, R.Y., Zhang, C.L., Sun, Y., 2013b. Crustal reworking in the North China Craton at ~2.5 Ga: evidence from zircon U—Pb ages, Hf isotopes and whole-rock geochemistry of the TTG gneisses in the Zhongtiao Mountain. Acta Petrol. Sin. 29 (7), 2265–2280.

Zhao, F.Q., 2006. Geochronologic and geochemical constraints on the Paleoproterozoic crustal evolution of Zhongtiao Mountains from Shanxi Province (PhD thesis) China Univ. Geosci., Beijing, pp. 31–77 (in Chinese with English abstract).
Zhao, G.C., Sun, M., Wilde, S.A., Li, S.Z., 2005. Late Archean to Paleoproterozoic evolution of the North China Craton: key issues revisited. Precambrian Res. 136 (2), 177–202.
Zhao, Y.R., Zhen, Y.Q., 2006. Genetic model for metamorphosed exhalative-sedimentary copper deposits of the Hujiayu–Bizigou-type in the Zhongtiao Region. J. Guilin Univ. Technol. 26 (3), 310–319 (in Chinese with English abstract).
Zhao, T., Zhai, M., Xia, B., Li, H., Zhang, Y., Wan, Y., 2004. Zircon U-Pb SHRIMP dating for the volcanic rocks of the Xiong'er Group: constraints on the initial formation age of the cover of the North China Craton. Chin. Sci. Bull. 49 (23), 2495–2502.
Zhong, R., Li, W., Chen, Y., Huo, H., 2012. Ore-forming conditions and genesis of the Huogeqi Cu—Pb—Zn—Fe deposit in the northern margin of the North China Craton: evidence from ore petrologic characteristics. Ore Geol. Rev. 44, 107–120.
Zhu, X., Zhai, M., Chen, F., Lyu, B., Wang, W., Peng, P., Hu, B., 2013. ~2.7 Ga crustal growth in the North China Craton: evidence from zircon U—Pb ages and Hf Isotopes of the Sushui complex in the Zhongtiao terrane. J. Geol. 121 (3), 239–254.
Zhu, Z.M., Sun, Y.L., 2013. Direct Re—Os dating of chalcopyrite from the Lala IOCG deposit in the Kangdian copper belt, China. Econ. Geol. 108 (4), 871–882.